PREVENTING PRESSURE ULCERS
BY PRESSURE DISTRIBUTION
VIA A LIQUID CRYSTAL ELASTOMER SMART SKIN

By

JEREMY PEREZ

Bachelor of Science in Mechanical Engineering
École Catholique des Arts et Métiers
67300 Schiltigheim, France
2016

Master of Engineering in Mechanical Engineering
École Catholique des Arts et Métiers
67300 Schiltigheim, France
2016

Submitted to the Faculty of the
Graduate College of the
Oklahoma State University
in partial fulfillment of
the requirements for
the Degree of
MASTER OF SCIENCE
July, 2021

PREVENTING PRESSURE ULCERS

BY PRESSURE DISTRIBUTION

VIA A LIQUID CRYSTAL ELASTOMER SMART SKIN

Thesis Approved:

Dr. Aurelie Azoug

Thesis Advisor

Dr. Yujiang (Mike) Xiang

Dr. Jerome Hausselle

ACKNOWLEDGMENTS

Thank you, Dr. Azoug, for supporting me during my thesis. You helped with the science when I needed it. You helped me get through 2020 when we all needed it.

Acknowledgments reflect the views of the author and are not endorsed by committee members or Oklahoma State University.

Name: JEREMY PEREZ

Date of Degree: JULY, 2021

Title of Study: PREVENTING PRESSURE ULCERS BY PRESSURE DISTRIBUTION VIA A LIQUID CRYSTAL ELASTOMER SMART SKIN

Major Field: MECHANICAL AND AEROSPACE ENGINEERING

Abstract: Pressure Ulcers (PU) are skin injuries costing an estimated 26 billion dollars per year. A sine qua non factor is prolonged pressure. Pressure from the body weight of hospitalized patients is enough to injure their skin and, without early action, can worsen and endanger patient life. One way to prevent pressure ulcers is to reduce the peak pressure on the skin to avoid ischemia. Liquid Crystal Elastomer (LCE) viscoelastic properties could make a Smart Skin, relieving pressure on the skin. To develop this Smart Skin, we will first explore the behavior of the skin under compression and, second, the behavior of the Smart Skin compressed by the weight of the body. In the first study, we aim at elucidating the link between mechanical loading and ischemia in the skin, considering the time-dependent properties of the skin. We model the skin microcirculation with a viscoelastic constitutive model and realistic blood vessels geometry to observe the impact of viscoelastic behavior on PU risk, quantified by a decrease in blood flow. A necessary condition to design a Smart Skin from novel LCEs is to predict their behavior reliably. In the second study, we developed and performed an experiment measuring the change in phase of the LCE under local compression. This experiment is then tentatively compared to a numerical simulation incorporating a dedicated constitutive model currently in development. These two approaches show the impact of time-dependence on the materials involved, whether biological or synthetic, in the decrease in blood flow and PU onset. They also show the impact of the nonlinearity of the LCE behavior on its behavior in compression.

TABLE OF CONTENTS

Chapter Page

LIST OF TABLES

LIST OF FIGURES

CHAPTER I

INTRODUCTION

A medical problem Pressure Ulcers (PUs), also known as bedsores, are skin injuries that occur whenever a weight presses on the skin for too long. They appear within a few hours, enough to do a little harm which heals without further issues if the skin is relieved. Indeed, They are benign in most cases but can become significantly worse if the weight persists or the injury is allowed to worsen. PU treatment costs billions of dollars each year in the US. Cost estimates keep increasing. A recent estimate reaches $26 billion, which according to the authors is conservative [34]. PUs commonly occur in facilities where patients are immobilized, such as hospitals. Indeed, hospitalized patients' skin supports their weight for as long as they stay in bed – sometimes for long as their hospitalization. An unfortunate combination of patients immobility with patients' unique conditions, weakening the skin, makes PUs a common occurrence in these facilities. PUs are just impossible to prevent in their entirety. However, it is not acceptable to let them worsen. Untreated, the skin eventually dies. Many cases are preventable, often attributed to negligence. Good PU prevention is an indicator of care quality. Thus, nurses routinely check for PUs while moving patients to relieve the skin. PU prevention guidelines, methods, and medical devices are constantly being updated and improved.

A mechanical problem Our understanding of PUs has vastly expanded over the centuries. We know of many pathways leading to PUs that are essential in PU prevention. Of the many PU factors, a prerequisite is always pressure. We observe, on immobilized patients, injuries with a similar appearance at locations where the skin supports the body weight pressure. A correlation undeniably exists between pressure, time, and PUs. Injuries that are not PUs might also occur and worsen where pressure is the highest. Pressure reduces blood flow in the skin. When the skin is not sufficiently fed blood, it dies. Our goal is not to accurately diagnose nor treat PUs. As mechanical engineers, we aim to give medical personnel a tool to distribute pressure. They will then judge when to use it appropriately. Pressure is not the only PU factor. PU is also not the only injury correlated with pressure. However, pressure is our focus in this study. We will additionally limit our scope to heel PU.

A mechanical solution With so many patients at risk, medical devices have been designed to relieve the pressure on the skin. Some pressure relief solutions are extreme, like mud beds to divide pressure over the whole body surface. Some are expensive, like self-moving beds to periodically relieve patient skin. Some solutions are simple, like cushions. Each has its use. They are to avoid pain and injury more than to be in any way comfortable.

Smart Skin Liquid Crystal Elastomers (LCEs) are smart materials, meaning they can change their properties according to their environment – to adapt. This adaptation grants them shape-memory behavior with temperature changes. Our Smart Skin aims to harness a different nonlinearity in their behavior, which changes mechanical properties under loading. LCEs contain liquid crystals. The rubber-like behavior of LCEs depends on the liquid crystalline structure. LCEs can transition from a solid-like to a liquid-like behavior as the liquid crystal molecules rearrange in the microstructure. This behavior change is called soft elasticity. Soft elasticity in tension corresponds to the liquid crystals aligning in the direction of the stretch. We are concerned here with compression. We will put the LCE in-between bed and body, pressing the LCE with the intent to lower the pressure on the skin. This sheet of LCE will effectively be a Smart Skin that can adapt to body shape and adapt its stiffness. Ideally, the LCE Smart Skin would provide a comfortable or efficient alternative to PU-preventing mattresses. However, many questions need answers regarding the LCE behavior.

Studies We divided this thesis into two studies: one about body skin behavior; one about LCE Smart Skin behavior.

In the first study, we aim at determining the influence of time-dependent phenomena in the skin on PU onset modeled as a reduction in blood flow. In the second study, we experimentally measure the LCE behavior in compression and set up a numerical simulation to evaluate a newly developed LCE model incorporating soft elasticity.

CHAPTER II

ISCHEMIA DUE TO VISCOELASTIC SKIN CREEP

2.1 Skin and pressure ulcers

2.1.1 Skin architecture

Skin is the largest organ in the human body [17]. Skin covers the whole body and has a vital role in protecting it against mechanical, physical, biological, and chemical hazards. Skin is composed of distinct layers: epidermis, dermis, and hypodermis (fig. 1). The epidermis is an avascular layer composed mainly of keratinocytes, which act as an environmental barrier. The epidermis is about 200 μm thick [27]. Keratinocytes are produced in the deepest part of the epidermis and migrate over four weeks to emerge dead in the top layer, the stratum corneum. The dermis is a vascular layer. Its volume is mainly ground matrix, a gel-like substance [27]. Under the dermis is the hypodermis, a tissue layer composed of fatty acids that offer additional protection.

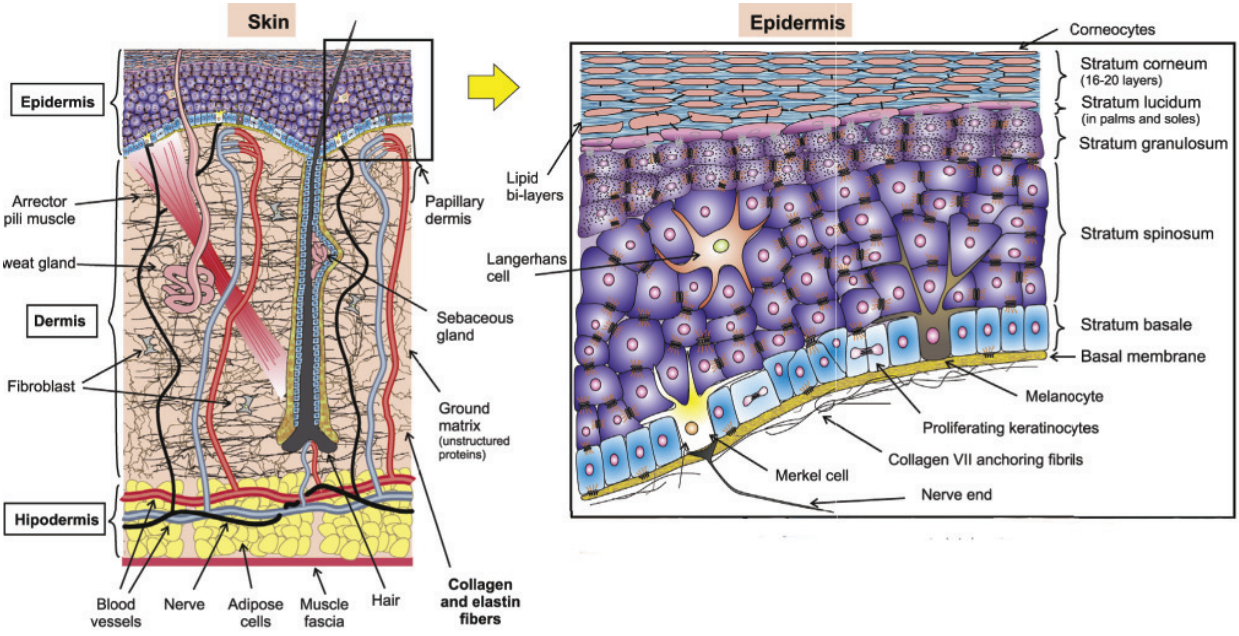

Figure 1: Detailed skin structure [8].

Skin properties and structure vary depending on location. This study focuses on plantar skin below the heel. As skin characteristics evolve to adapt to stress and prevent damage [18], plantar skin is thicker than skin in other locations [8]. Observed values for epidermis

thickness in plantar vary within a range of 800-1500 μm [8] and a thickness of ≈ 600 μm has been measured on the heel pad [13].

Microvasculature For organs to function properly, they must receive a steady blood supply, bringing oxygen and nutrients. Skin microvasculature is found in the dermis (fig. 2). Living cells in the epidermis rely on diffusion to get nutrients. Oxygen has to reach the whole volume. Thus skin microvasculature has to be space-filling. Blood is transported to the dermis through an ascending plexus of arterioles and evacuated through a descending plexus of venules [11]. The ascending plexus ends as arterioles reach the stratum basale and form capillary loops feeding a descending venule plexus. Capillaries are blood vessels of internal diameter lower than 7 μm, where the flow is very different from Poiseuille flow. Capillaries will not be included in our vasculature model as we do not envision them directly impacting the onset of pressure ulcers.

Figure 2: Skin microvasculature illustration[12]

2.1.2 Skin mechanical behavior

The dermis is larger than the epidermis and is responsible for most of the skin viscoelastic mechanical properties [27, 33]. Due to its structure, the mechanical behavior of the skin in tension and compression is different. Dermis properties in tension largely depend on the collagen fibers in the extracellular matrix [27]. In compression, properties depend on the ground matrix [8]. Characterizing skin mechanical properties is challenging. Skin mechanical properties depend on individuals and location. In addition, testing methods tend to affect the measurements as skin is a living material that degrades quickly outside of the body [33, 22]. It is not in the scope of our study to provide a structural model considering the intricacies of

the skin as a composite material. Thus we modeled the skin as a linear viscoelastic material and identified material parameters on experimental data obtained on a human cadaver heel pad.

2.1.3 Pressure Ulcers

Other names PUs have been diagnosed for at least 5000 years [3]. Although PU is currently the prevalent name [10], this condition has gotten many names such as Pressure Injuries (PIs), bedsores, decubitus ulcers, pressure sores, pressure necrosis, ischemic ulcers, heel ulcers, sacral ulcers. The list before is not exhaustive.

Definition In 2016, the National Pressure Injury Prevention PANEL (NPIAP) has defined PIs – which we refer to here as PUs – as "localized damage to the skin and underlying soft tissue usually over a bony prominence or related to a medical or other device" .

Hence, the injury is pressure-related, but the skin does not have to be ulcerated, which is the case in the early stages of PUs [15]. We will refer to that definition, which excludes damage due to clothing or skin friction and includes nondescript terms such as 'bedsore', literally a lesion due to a bed, and 'decubitus ulcers', literally ulcers caused to patients laying down, that is in the decubitus position.

We consider the term PU most relevant for our study and the given definition by the NPIAP most appropriate.

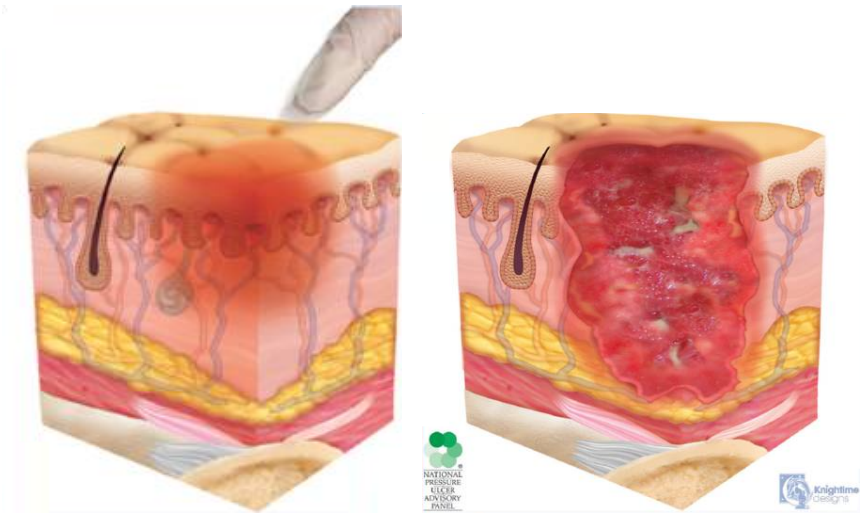

(a) Stage 1: Non-blanchable redness

(b) Stage 3: Ulceration

Figure 3: Different stages of PU progression [15]

Ischemia Ischemia, *i.e.* the lack of blood supply, is the main cause of pressure ulcers (PUs) [3]. Ischemia occurs when the skin is under excessive pressure for prolonged times, which is purposefully a vague definition of the threshold as the actual values vary with patients and their health conditions. Ischemia is arbitrarily said to occur around the ischaemic pressure,

at 4.3 kPa (32 $mmHg$) [7], determined from a skin capillary pressure measured in 1930. This threshold is generally reached under a bony prominence because the lack of adipose tissue concentrates pressure on a limited area, leading to high compressive stresses on the skin. The ischemia leads to an acute inflammatory response. This response can allow the tissue to recover (healing) or become self-maintaining and excessive, resulting in the onset of PU [48] (fig. 3).

Ulceration An ulcer is defined as a break in the skin or mucous membrane with loss of surface tissue, disintegration, and necrosis of epithelial tissue, and often pus [28].

Thus, PUs do not start as ulcers. PU development is indeed categorized into four stages. Stage 1 PUs can be detected on observation of a non-blanchable redness over intact skin (fig. II.3(a)) though the patient would often feel pain before that. Skin ulceration instead occurs at later stages (fig. II.3(b)) as necrosis continues toward deeper tissues [15]. PUs staging is different from other wounds and ulcers, though some can have specific similarities. For example, the diabetic foot ulcer [15] shares similar pathogenesis, thus pressure relief has a positive impact on its recovery [44].

PUs are often classified as chronic wounds as they do not recover via the normal process of wound healing as acute wounds would. Partial and full skin loss must be treated using a treatment plan unique to each patient. The treatment plan should attempt to root out the causes of the wound, debride the dead tissues to obtain an acute wound, then dress the wound and help recovery [9]. PU treatment is intensive and puts a heavy burden on both patients and health care systems.

Quantifying Pressure and Time dependence A lower limit for PU development is ischemic pressure. In 1976, Reswick and Rogers published a recommendation curve based on 980 medical observations in which they highlighted the pressure-time dependence for PU formation under bony prominence. They suggested acceptable and unacceptable skin pressures from a bony prominence as a function of time. Higher pressures are acceptable for shorter times. The guidelines were not intended to give an exact PU threshold. Indeed, there is an undefined area between acceptable and unacceptable parameters (fig. 4). In supine, the maximum pressure of 23.3 kPa (175 $mmHg$) is located under the sacrum pressure. Pressure under the heel is about 20.0 kPa (150 $mmHg$) [19]. These guidelines suggest PUs might occur within three hours. Patients have developed PUs within four hours in supine [43].

2.1.4 Prevention

Most pressure ulcers are avoidable [23]. Practices can limit common causes of PUs. Healthy individuals are prevented from developing chronic wounds simply by moving as soon as pain occurs before or during stage 1 PUs. Additionally, while the definition of discomfort can be subjective [14], it is associated with pain. Thus individuals are expected to maintain a behavior to limit the pain and thus prevent PUs.

Patients may, however, behave differently. Hypoesthesia may negate PU pain, paralysis may prevent pressure relief, lack of activity may lead to weaker tissues, and poor mental health may lead to generally unhealthy behaviors. All may increase the risk of PUs [9].

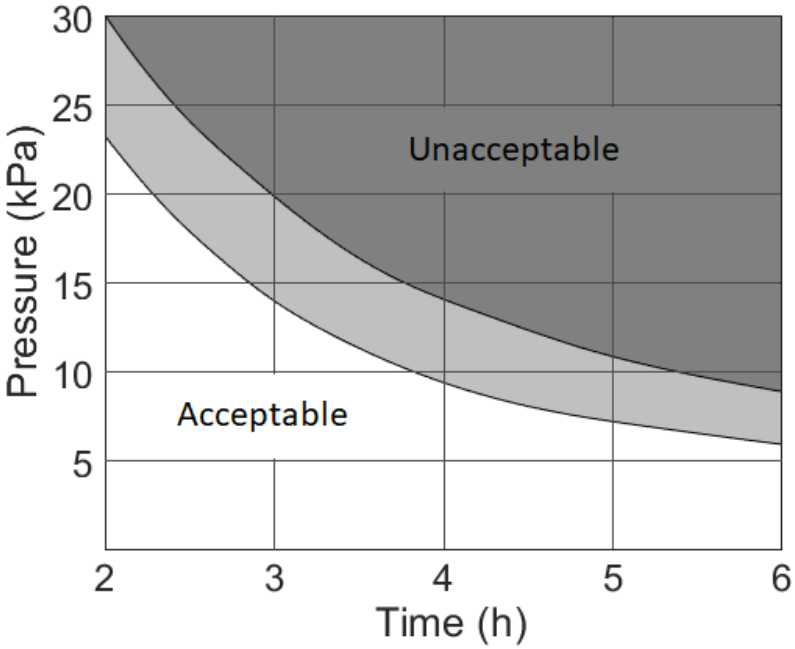

Figure 4: Acceptable pressure vs time. Adapted from Reswick and Rogers guidelines [38]. Guidelines before 2 hour and after 6 hours were excluded.

Supports are thus designed to lessen the pressure on the skin. Patient guidelines also encourage nurses to regularly move patients as well as monitor them for PUs signs. Current guidelines suggest turning patients at risk of PUs every two hours, though compliance to that rule is usually below 60% [35]. Excessive skin moisture, skin friction, low oxygen, impaired healing, poor nutrition [9] are additional risk factors that can be lessened. PU prevention will remain an active research topic for as long as they remain a common and expensive occurrence.

2.1.5 Epidemiology and cost

Patients in facilities have a high risk of developing PUs (table 1). An estimated 2.5 million US patients develop a PU each year [34]. Among PUs acquired in facilities, stage 1 PUs are most frequent (table 2). Individuals may develop PUs in beds, wheelchairs, or from then contact with a medical device [15]. Elders constitute 70% of PUs patients [3] and 80% of PUs deaths [37]. An estimated 60 000 US patients die from PU each year [34].

Location	PU incidence
Inpatient Dept.	0.4-38%
Long-Term Care Facilities	2.2-23.9%
Home Care	0-17%
Spinal Cord Injury (1^{st} month)	30-85%

Table 1: Reported PU incidence according to facility [3]

Stage	Incidence
1	5.2%
2	2.1%
3-4	1%

Table 2: Estimated PU incidence in US hospitals [34]

PUs were estimated a few years ago to cost $11 billion per year [32]. Estimations have kept increasing. Currently, US spending are estimated to directly cost $26.8 billion per year, at an average of $10,708 per patient [34], with treatment costs ranging from $500 to $70,000 [32]. Stage 1 PUs are usually on the lower end, while later PU stages cost may vary greatly depending on the nature of the stay [34].

2.2 Motivation and Objectives

This study aims at modeling PU onset in a time-dependent mechanical model. The knowledge of PUs mostly comes from medical professionals whose preoccupation is to prevent and treat PUs. We cannot use guidelines from medical observations as their purpose has always been to share knowledge between medical professionals with the same preoccupation. In our case, we look to create an injury – in a simulation.

We need to know how much pressure we can apply on a human heel before injury occurs. We thus also need an objective mechanical threshold we can use to detect it. These will allow us to evaluate the performance of our Smart Skin as well as contribute our new knowledge to PU research.

With our knowledge of the viscoelasticity of the skin, we can build a model using the viscoelastic properties of heel skin. We can build blood vessels using other studies detailing their geometry. Studies on fractal trees exist. However, to the best of our knowledge, none have used a fractal tree in a viscoelastic simulation.

Objectives

- Knowledge on viscoelasticity:
  Understand the exact impact of viscoelasticity in PU formation.

- Realistic skin model:
  Calibrate our constitutive law to accurately model live heel skin in creep during 2 to 4 hours at 5-25 kPa.

- Realistic skin with vessel:
  Mesh a vascular heel skin to use in a simulation with a constitutive model.

- PU detection:
  Set an objective threshold to detect injury risk or presence.

- Smart skin evaluation:
  Get an admissible pressure range for Smart Skin pressure distribution

2.3 Simulation Method

2.3.1 Fractal tree model

Fractal geometry has been used to model vascular networks [31, 39, 40]. Arteriole and venules networks can be viewed as fractal trees. To obtain a realistic geometry, we applied West et al. [45] 3 principles to model transportation of essential materials – blood in our case. Our fractal ended at a size-invariant unit; the capillary size. Our geometry was a space-filling branching fractal. Our energy to distribute blood was minimized; through Murray's laws.

Blood circulates through systemic – heart/capillaries – and pulmonary – heart/lungs – systems and are associated with different models and parameters [31]. These can also change depending on the organ. We selected what could be applied to the heel skin while possible. Skin blood vessel trees have been observed in the chest, back, and abdomen (fig. 5). We were not able to procure a representation of heel skin blood vessels for comparison. Following the work of Sree et al. [39] we modeled the microvasculature of the upper part of the tree in the 10-30 μm range. We thus set an initialization diameter $D_0 = 30\ \mu m$.

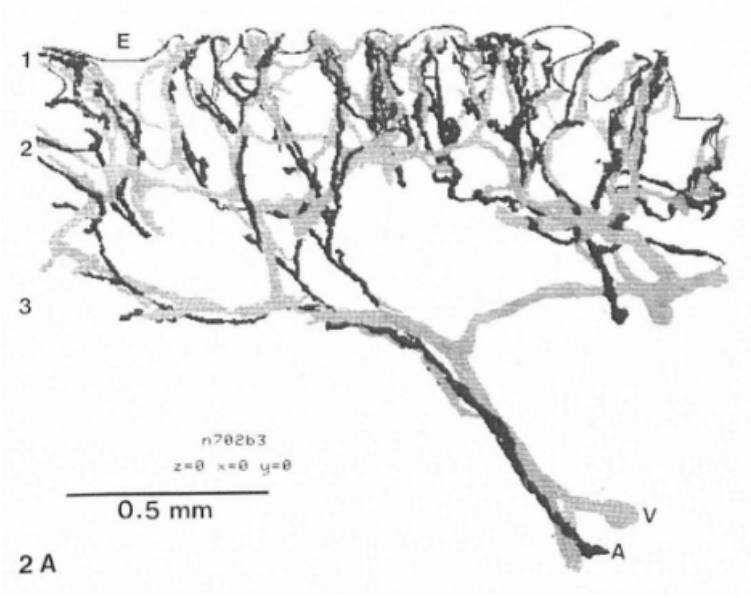

Figure 5: Skin blood vessel venal (V) and arterial (A) trees [11]

Final branch Branching stopped at $d_{end} = 10\ \mu m$ which is near equal to capillary diameter [39]. Capillary size–diameter–is independent of body size [45].

Space-filling branching fractal Any parent branch P could divide in two branches $D1$ and $D2$. Branch lengths l were scaled with branch diameters d using the allometry relation [40]:

$$l = Ad^B$$

With $B \approx 1.0$. We thus obtained:

$$l_{D1/2} = \left(\frac{d_{D1/2}}{d_P}\right) l_P$$

In our tree, the relative length reduction is thus the same as the diameter reduction. Initial length was arbitrarily chosen to visually match with fig. 5.

$$l_0 = 24.5 d_0$$

We built curved branches. To make curves, we divided branches into ten equal-length sections. We generated each section direction using a different direction we obtained from three contributions as in Sree et al. [39].

Energy minimization We applied Murray's Law to lower energy loss in a Poiseuille's flow. It gives us the relationship between the parent branch diameter d_P and its daughters d_{D1} and d_{D2} using an exponent m [30]:

$$d_P^m = d_{D1}^m + d_{D2}^m$$

The law is scale-invariant and has been used empirically to model limbs by da Vinci [1] and botanical trees by Murray [30] with various exponents. Murray demonstrated $m = 3$ optimized blood flow. Observations sometimes differ from Murray's Law with m values slightly below three [40, 31]. We arbitrarily chose to follow Murray's Law with $m = 3$ to obtain a geometry.

Direction cosines α_{D1} and α_{d2} of the angles with the parent branch were given using an optimisation given in another of Murray's papers [29]:

$$\alpha_{D1} = \frac{d_P^4 + d_{D1}^4 - d_{D2}^4}{2(d_P d_{D1})^2}$$

$$\alpha_{D2} = \frac{d_P^4 - d_{D1}^4 + d_{D2}^4}{2(d_P d_{D2})^2}$$

In 1975 Zamir proposed multiple optimization for branching angles [47]. Murray's angles correspond to an optimization of blood volume per unit of length for bifurcations. Other possible optimizations are surface, power and drag force per unit of length. Our choice is arbitrary.

Blood vessels may have an asymmetrical branching or Y-shaped symmetrical [24]. From Murray's laws, if $d_{D2} = d_{D1}$ we obtained:

$$\frac{d_{D1}}{d_P} = 2^{-1/3} \approx 0.79$$

$$acos(\alpha_{D1}) = acos\left(\left(\frac{1}{2}\right)^{1/3}\right) \approx 37.5^\circ$$

If $\frac{d_{D1}}{d_P} \to 1$ then:

$$acos(\alpha_{D1}) \to 0^\circ$$

$$acos(\alpha_{d2}) \rightarrow 90^{\circ}$$

We chose to limit the range of the values using an equation inspired by the work of Adjoua *et al.* [1]:

$$d_{D2} = kd_P$$

Where k is assigned a random value between 0.65 and $2^{-1/3} \approx 0.79$. This allowed for symmetric bifurcation while staying close to Adjoua *et al.* parameters [1].

Rotation of the bifurcation around the parent branch is free and given an arbitrary value between 0 and 2π.

2.3.2 Fractal tree generation and mesh

Fractal algorithm We wrote an algorithm to build the random fractal tree with object-oriented programming in MATLAB (The MathWorks, Natick, MA, USA). The Tree object is composed of Branch objects, composed of an array of equidistant nodes and a diameter value. We show the structure in figure 6.

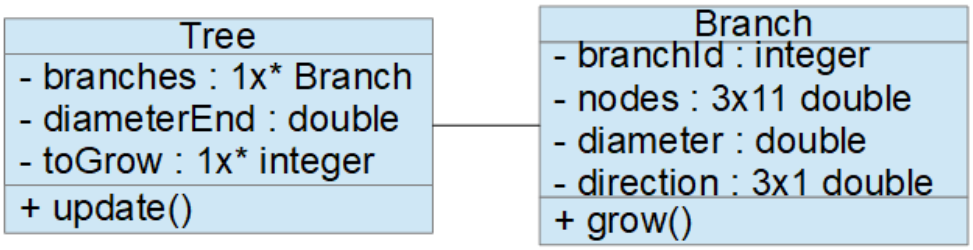

Figure 6: Simplified Unified Modeling Language diagram for the construction of the fractal tree representing the blood vessel.

The tree was initialized with a single 30 μm diameter branch and grown according to the flowchart presented in figure 7. Tree generation terminated when there were no more branches to grow. Each grown branch would split into two children unless the parent branch collided with another branch or the child diameter were less than 10 μm – capillary size.

We detailed the parameters and equations we used in the previous section. We arbitrarily chose some parameters to visually match Braverman's tree (fig. 5).

Tree geometry We wrote a MATLAB script to print a meshing software script that would generate a geometry. We tried at first to generate a SOLIDWORKS (Dassault Systèmes, Vélizy-Villacoublay, FRANCE) geometry. However, meshing was not successful and highlighted the need to build a geometry using simple elements. After more trial and error, we then chose to build the final geometry (fig. 8) using the open-source software Gmsh [16] version 4.8.4 with a specific strategy.

We defined the tree volume using a set of closed surfaces. To allow automation, we introduced three geometry families to define the surfaces: Branch, Branching, and Reducer. A parent Branch would connect to its children through a Branching or a Reducer. Each Branch was composed of two half-sections, each defined by four surfaces (fig. II.9(a)). At mid-length,

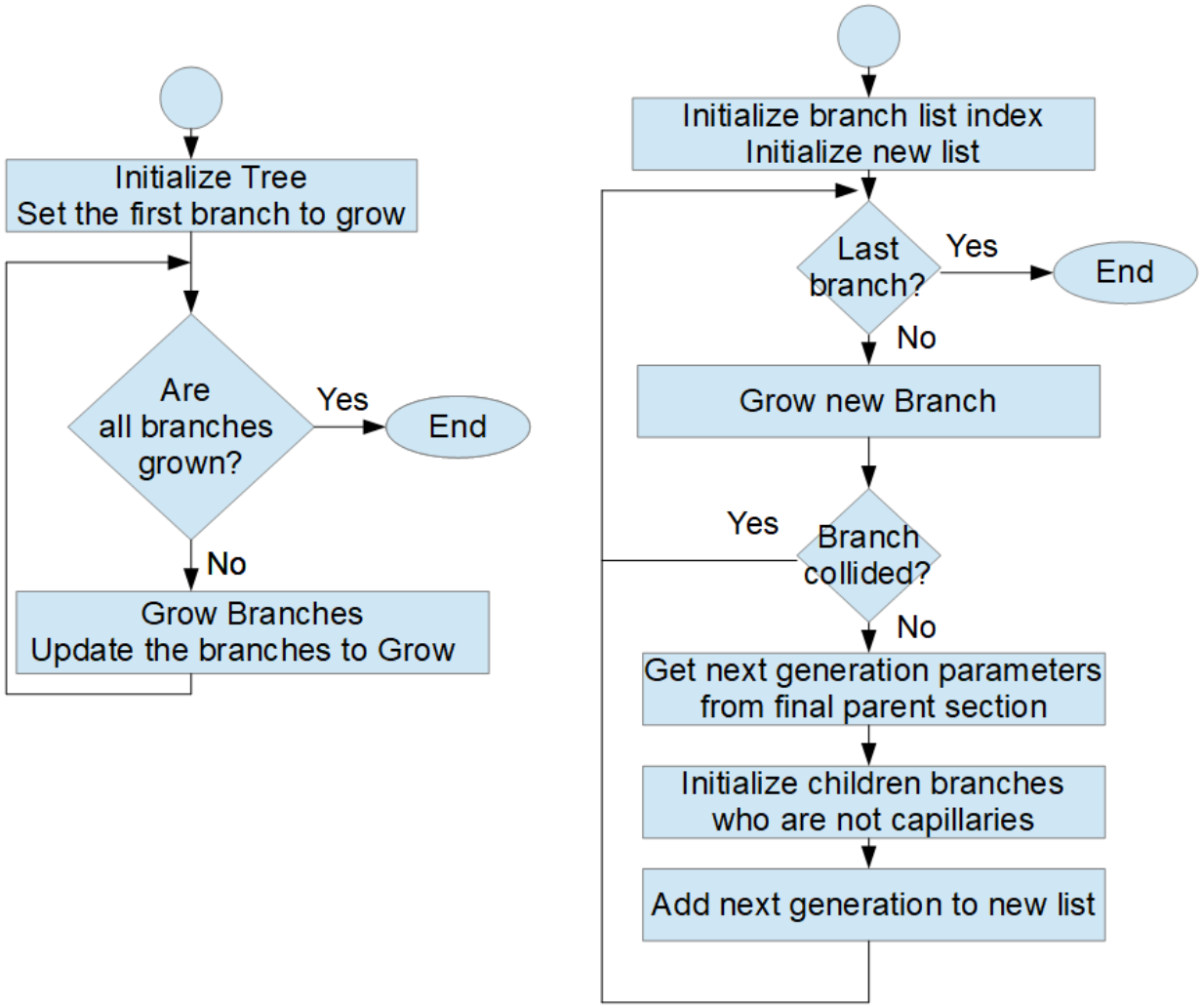

Figure 7: Simplified flow chart of the tree and branches generation.

additional points allowed a rotation of the two midsections. Some Branches were curved, and midsections would help the meshing algorithm interpret the surfaces correctly. Each Branching connected three Branches with different diameters. We defined them via eight convex surfaces (fig. II.9(b)). Each Reducer connected two Branches of different diameters. We defined them with four convex surfaces (fig. II.9(c)). The 3D volume was defined from 0D points successive Gmsh functions (table 3). Meshing was successful and allowed for easy radius detection later, so we kept the strategy though it can surely be improved.

After obtaining the tree geometry representing our blood vessels, we placed it inside a cubic volume representing the dermis. We subtracted the tree from the volume to obtain the skin geometry. The sides of the cube were chosen sufficiently far from the microvasculature. We made the avascular part at the top of the skin as large as the heel epidermis thickness.

We meshed that geometry using Gmsh default parameters and transferred nodes and connectivity into Feap format via a script. The whole geometry is meshed with tetrahedron elements, combining the two materials. We limited the number of nodes and elements. We obtained edges at branch cross-sections with 1, 4, or 6 nodes.

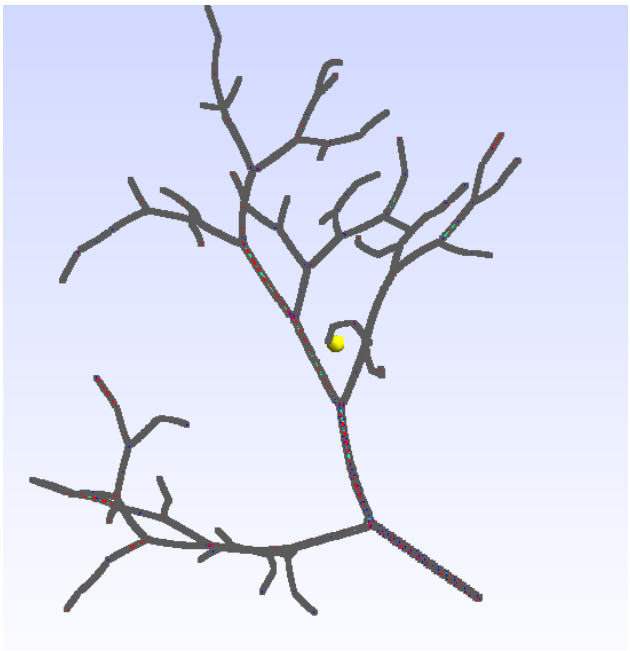

Figure 8: Tree Geometry

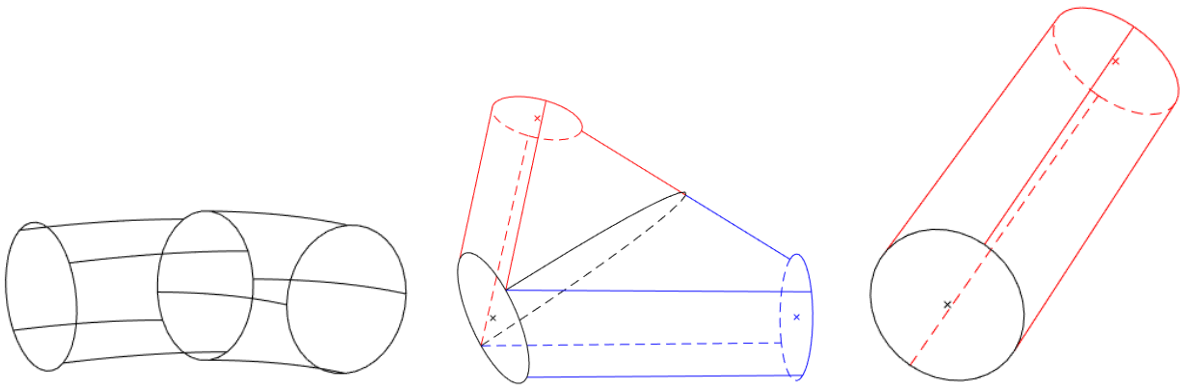

(a) Branch Element surfaces (b) Branching Element surfaces (c) Reducer Element surfaces

Figure 9: Element surfaces

Function	Output	Arguments
Point	Point	XYZ Coordinates
Line	Curve	2 Points
Spline	Curve	N Points
Curve Loop	Closed Path	N Curves
Surface	Plane Surface	Closed Path
Surface	Surface	Closed Path
Surface Loop	Closed Surfaces	N Surfaces
Volume	Volume	Closed Surfaces

Table 3: Used Gmsh functions

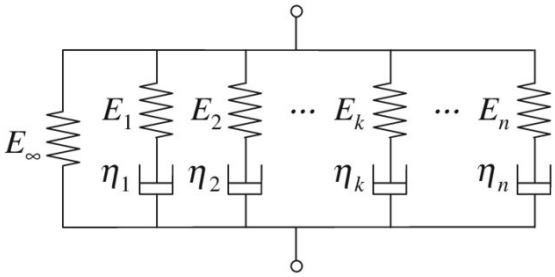

Figure 10: Generalized Maxwell model with n elements, where E_∞ is the equilibrium modulus, and E_k and η_k are the modulus and viscosity of element k.

2.3.3 Blood vessel material properties

Blood vessels were modeled as linear elastic with a modulus of 4.3 kPa corresponding to the ischemic/capillary pressure [40]. Their pressure is below arteriole pressure and above venule pressure. The Poisson ratio was chosen to reflect compressibility ($\nu = 0.2$).

2.3.4 Skin viscoelastic model and parameters

We chose a generalized Maxwell model (fig. 10) to represent the viscoelastic behavior of the skin. We used the constitutive law associated with the model as described in equations (2.3.1) and (2.3.2).

$$\sigma(t) = \int_0^t E(t-s)\dot{\varepsilon}(s)ds \tag{2.3.1}$$

$$E(t) = E_\infty + \sum_{k=1}^{n} E_k e^{-t/\tau_k} \tag{2.3.2}$$

where σ is the stress, t the time, $E(t)$ the relaxation modulus, ε the strain, E_∞ the equilibrium modulus, E_k and τ_k the modulus and relaxation time associated with Maxwell element k, and n the number of Maxwell elements in the model.

This model was fitted on experimental data from the literature [25]. The experimental study [25] was chosen because it comprehensively characterized the viscoelastic behavior of plantar tissues in compression. Skin specimens were excised from cadaver feet. The plantar

tissue was tested in compression during uniaxial and stress relaxation tests. We focused on the measurements performed on the subcalcaneal region, namely the heel pad.

Tissues were cut into 2 cm by 2 cm specimens. All specimens were preconditioned with 10 sine waves to the target displacement at a frequency of 1 Hz. The stress-strain cyclic curve was measured at a frequency of 10 Hz, that is a strain rate of 10 s^{-1}, which is relatively fast for quasi-static testing (fig. II.11(a)). For the stress relaxation measurement, the tissue was compressed to the target displacement over a period of 0.1 s and held at a constant strain for 300 s (fig. II.11(b)).

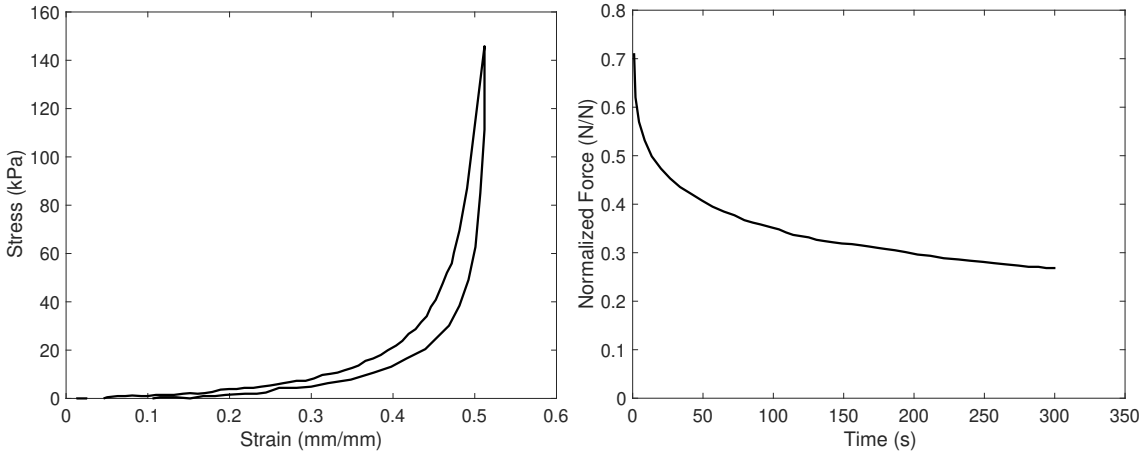

(a) Stress-strain curve (b) Stress relaxation

Figure 11: Experimental characterization of subcalcaneal tissue in compression, data from [25]

We fitted the normalized relaxation modulus of the generalized Maxwell model directly on the experimental relaxation curve with a least-squares method. The fit was performed in MATLAB using a trust region reflective algorithm and tolerance of 10^{-8}. We then identified Young's modulus on the uniaxial compression loading curve below 40% strain using another fit. This strain range is relevant to the compression range we are aiming at simulating in this study. As the modulus increases drastically above 45%, this limit was necessary not to overestimate the modulus of the skin at low compression levels.

2.3.5 Other simulation parameters

Boundary conditions We applied pressures of 2.5, 5, 10, or 15 kPa on the skin's surface, normal to the X-axis in our mesh. We chose values around the ischemic pressure. We chose one point at the bottom of the dermis and made it unable to move in any direction. We then prevented the bottom of the dermis from moving in the X-direction.

Time We simulated the deformation from $t_0 = 0$ to t_f. To best observe the time-dependent deformations, we chose t_f to be more than three times our maximum relaxation time in the Maxwell model. We also used an adaptive time step. We set the first time step at t_1 to be less than a tenth of the lowest relaxation time.

2.3.6 Detecting blood vessel blockage

Our objective when simulating skin creep was to detect blood vessels blockage. A reduction in radius will increase flow resistance. In a Poiseuille flow, the volume flow rate is proportional to r^4[30]. For example, a 33% radius reduction from an initial radius r_0 would reduce the volume supplied by 80%. We estimated that this reduction in blood flow was enough to initiate skin cell damage. We considered the blood vessel blocked if $(r(t) - r(t_0))/r(t_0) < -33\%$. In our simulation, blood vessel cross-sections did not shrink as they needed radial pressure to pull their wall inside. Instead, circular cross-sections deformed into elliptic cross-sections. We thus use $r = min(a, b)$ with a and b the semi-major/semi-minus axis of the ellipse. A similar study to ours used the cross-sectional area [26].

Circle and Ellipse Fitting We fitted circles and ellipses on discrete nodes. For each fit, we obtained a center C, normal d, and the radius r or a and b. To fit a circle we projected the nodes on a plane of normal d then numerically solved the equation $1 = (X^2 + Y^2)\frac{1}{r^2} + (-2X)C_x + (-2Y)C_y$ using the (X, Y) coordinates of the projected cluster points. This equation was obtained by developing the circle equation after neglecting the $\frac{C_x^2+C_y^2}{r^2}$ term. Circle fitting was used on the initial mesh. For the deformed geometry, we used an ellipse equation $1 = (X^2)\frac{1}{a^2} + (Y^2)\frac{1}{b^2} + (-2X)C_x + (-2Y)C_y$.

Clustering Because we created our geometry from elementary surfaces sharing curves with branch radial edges, we could quickly obtain node clusters that included circle edge points. We first grouped each node with its nearest branch point from our fractal to select those points for circle fitting. Then, we eliminated points that did not fit a circle and obtained several clusters shaped as circles (fig. 12). Each cluster was thus associated with a unique fractal tree branch ID $branchId$, allowing us to access all fractal tree branch property $[PROPERTYNAME]_{branchId}$. We reused the clusters detected in the initial mesh on the deformed meshes.

Measurements and plots We fitted an ellipse on each cluster. The effective radius of the vessel was determined as the minor radius of the ellipse $r(t) = min(a(t), b(t))$.

We obtained the direction cosines $\underline{d(t)} = [cos(\theta_x), cos(\theta_y), cos(\theta_z)]$. Because we compressed in the X direction, we precisely looked at the direction cosine $cos(\theta_x)$ and θ_x and we simply refer to θ_x as θ.

We obtained the coordinates $C(t) = [x_C(t), y_C(t), z_C(t)]$ of the center of the ellipse and looked particularly at $x_C(t)$ because of our boundary conditions and first branch direction. We simply referred to $x_C(t)$ as $x(t)$.

For time-dependent variables, we used the subscripts 0, 1 and f to designate the variable at t_0, t_1 and t_f. For example, $r_0 = r(t_0)$. We plotted the evolution of radii according to time. We defined the radius change as $\frac{r(t)-r_0}{r_0}$. We also defined the value excluding the contribution from the instantaneous deformation $\frac{r(t)-r_1}{r_0}$. We plotted the directions against time as it had been shown to be a factor of vessels collapse [39]. We used scatter plots to visualize correlations between measurements.

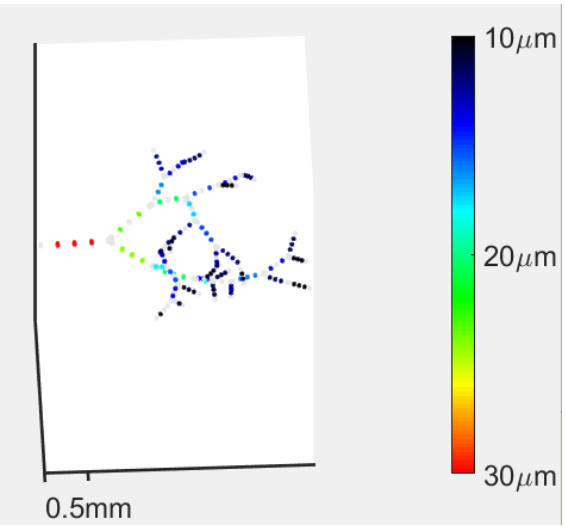

Figure 12: Clustering on blood vessel nodes. Gray nodes are excluded from diameter measurement.

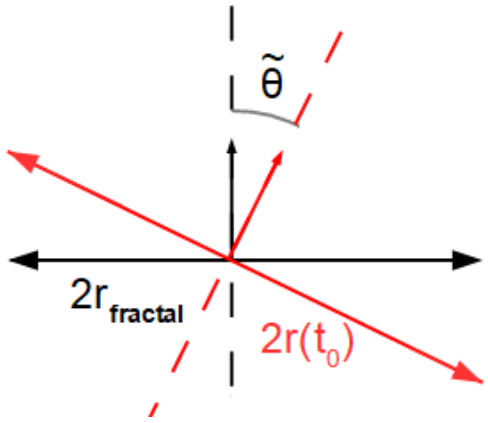

Figure 13: Fractal cross-section (black) were compared with computed mesh cross-section (red). Ideally, $\epsilon = |r(t_0) - r_{fractal}| = 0$ and $\widetilde{\epsilon} = 1 - |cos(\widetilde{\theta})| = 0$.

Error Measurement We compared the measurements at t_0 with fractal tree properties. For radii, we compared the fit value $r(t_0)$ from from the fractal value $r_{fractal} = diameter_{branchId}/2$. Directions could not be compared directly so we approximated a direction $\underline{\tilde{d}}$ using the fractal tree branch nodes nearest point and compared it with $\underline{d(t_0)}$ using a dot product $\underline{d(t_0)} \cdot \underline{\tilde{d}} = cos(\tilde{\theta}) \approx 1$ (fig. 13). We obtained the values $\epsilon = |r(t_0) - r_{fractal}|$ and $\widetilde{\epsilon} = 1 - |cos(\widetilde{\theta})|$ to represent how accurately we detected radii and cross-section normal directions. We then calculated their mean (μ_ϵ, $\mu_{\widetilde{\epsilon}}$), standard deviation ($\sigma_\epsilon$, $\sigma_{\widetilde{\epsilon}}$) and maximum value to represent their distribution.

2.4 Results and discussion

2.4.1 Skin mechanical properties

The generalized Maxwell model (equ. (2.3.1)) was fitted on literature experimental measurements (fig. 14). We detailed the parameters we obtained for the model in Table 4. The fit showed that three Maxwell elements were sufficient and necessary to predict stress relaxation measurements correctly.

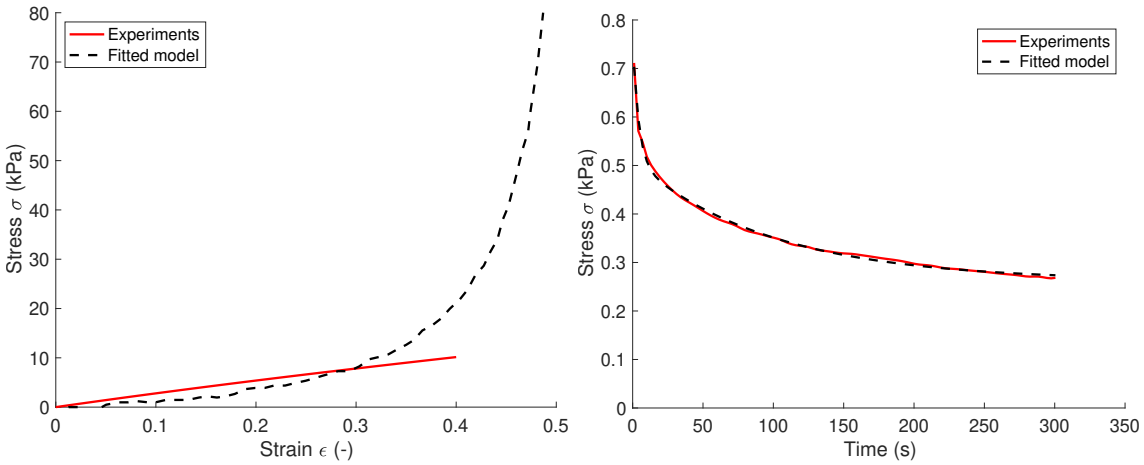

(a) Fit of the stress-strain curve

(b) Fit of the stress relaxation curve

Figure 14: Generalized Maxwell model fitted on experimental measurements of subcalcaneal skin

Parameter	Fitted Normalized Value (-)	Final Absolute Value (kPa or s)
E_∞	0.26	24.73 kPa
E_1	0.42	10.32 kPa
τ_1	-	0.041 s
E_2	0.25	6.14 kPa
τ_2	-	4.2 s
E_3	0.25	6.14 kPa
τ_3	-	97.5 s

Table 4: Parameters of the fitted Maxwell model with three elements

The fit of the generalized Maxwell model on the stress relaxation data (fig. II.14(b)) was excellent, indicating the skin viscoelasticity remains linear at these strain levels and times. Our linear viscoelastic model did not predict the compression stress-strain behavior equally well (fig. II.14(a)). Like most soft tissues, the skin exhibits a highly nonlinear behavior in tension and compression where the modulus increases drastically at a strain threshold marking the end of the small strain region and the beginning of a large strain one. This nonlinearity corresponds to the limit of rearrangement mechanisms and the transition to

applying loading directly on cells and molecules. Nonetheless, the skin stress response and its time-dependency are appropriate for our purpose, where we simulate the skin as the medium in which resides the blood vessel.

2.4.2 Blood vessel geometry

We implemented the branch growing algorithm proposed by Sree *et al.* [39]. We built the fractal on the assumption that the tree had to be space-filling. We added two additional assumptions – scale-invariant termination condition and optimization. Termination at capillary diameter is less arbitrary than termination as a fixed generation and allows the tree to start at any diameter. Energy optimization results in branching rules with more realistic angles. The suggested length reduction of 40% [39] (k=0.6) is on the lower end of our 0.65-0.79 range. However, information on skin blood vessels is sparse, and the exact value k for heel skin is unknown and probably subject-dependent. The obtained geometry (fig. 15) is similar to available direct images of skin blood vessels.

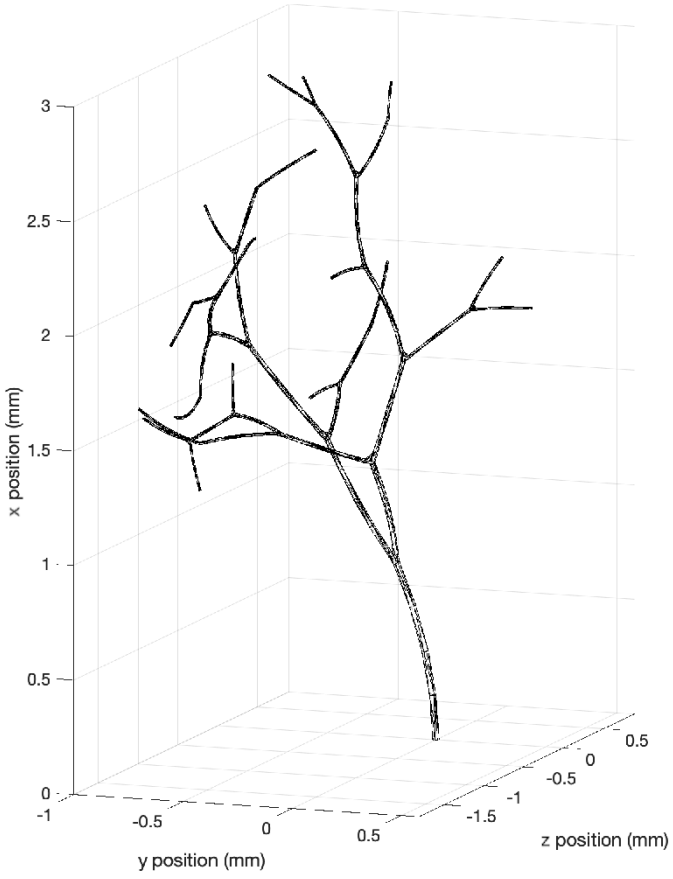

Figure 15: Microvasculature mesh

We chose several arbitrary values as well as random parameters to build the fractal. We

do not expect to link all of them to a physical value or principle due to the chaotic nature of living materials. However, we could use more statistical data to compare our tree with observations. We additionally remarked that this geometry allowed us to obtain uniformly distributed angles and radii (fig. 19).

2.4.3 Diameter Reduction

Cross-section orientation at t_0 We first checked the accuracy of our cross-section detection algorithm. Absolute radius error were several orders of magnitude lower than the 10-30 μm range. The cosines of the angles between cross-section normal and estimated normal were all close to 1. We obtained negligible errors and validated our method (table 5).

Radius (μm) $\epsilon = \lvert r_0 - r_{fractal} \rvert$			Cosine ($-$) $\widetilde{\epsilon} = 1 - \lvert cos(\widetilde{\theta}) \rvert$		
μ_ϵ	σ_ϵ	$max(\epsilon)$	$\mu_{\widetilde{\epsilon}}$	$\sigma_{\widetilde{\epsilon}}$	$max(\widetilde{\epsilon})$
$2.0.10^{-4}$	$1.4.10^{-4}$	$7.1.10^{-4}$	$1.6.10^{-5}$	$8.3.10^{-5}$	$8.2.10^{-4}$

Table 5: Measurement errors at t_0. μ and σ are the mean and standard deviation of the distribution of ε.

We observed some non-negligible errors at times higher than t_0. Since results were computed at 119 cross-sections from 40 branches at 28 time-steps, these errors were not overall significant.

Radius Reduction at P=2.5 kPa The objective was to determine the evolution of vessels radii with time. Due to the random properties of our tree and branches, the plots cover a surface between two bounds. (fig. 16). Radii both increase and decrease according to branch properties (fig. II.16(a)). Viscous deformation, represented by the normalized radius reduction, is non negligible (fig. II.16(b)).

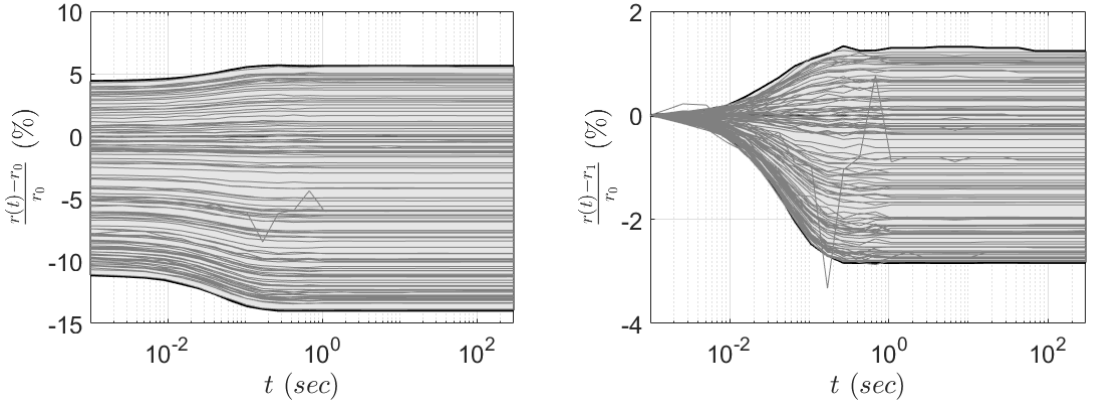

(a) Radius reduction including the instantaneous deformation at t_1

(b) Normalized radius creep, excluding instantaneous deformation

Figure 16: Radius reduction versus time at p=2.5 kPa.

Diameter reduction at different pressures We compared the bounds of radius reduction for different pressures (fig. 17). A pressure of 5 kPa, just above ischemic pressure, created a maximum radius reduction of 27.64%, near the 33% threshold we set for hypoxia. While the result is believable, we would refrain from concluding 5 kPa on PUs due to the approximations in our model. Nonetheless, the model shows that a large instantaneous displacement can be responsible for crossing the hypoxia threshold at higher pressure. At lower pressure, a non-negligible viscoelastic effect may instead be responsible for crossing that threshold (fig. II.17(b)). The shape of the curve appeared highly dependent on dermis deformation and, hence, on the dermis model. Cross-section displacements had a similar shape (fig. 18).

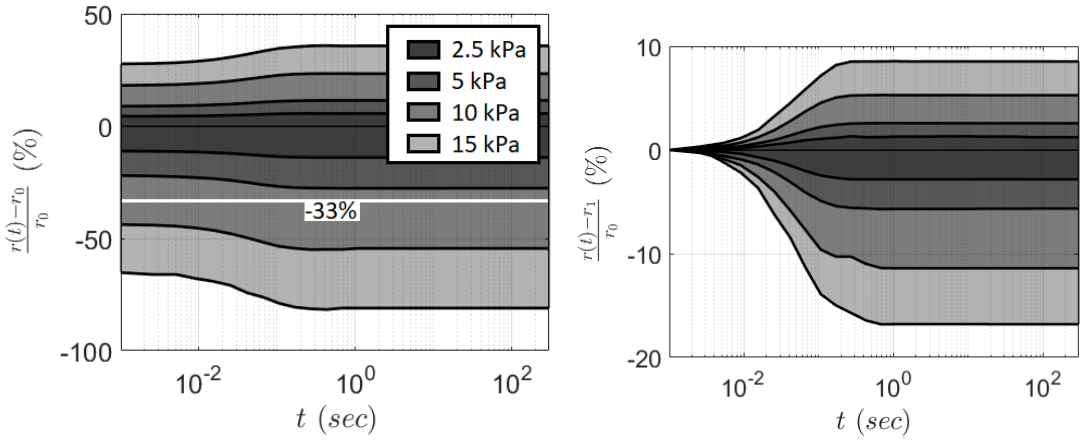

(a) Diameter reduction

(b) Instantaneous deformation excluded

Figure 17: Radius reduction versus time at p=[2.5, 5, 10, 15] kPa. The white line represents the -33% ischemia threshold.

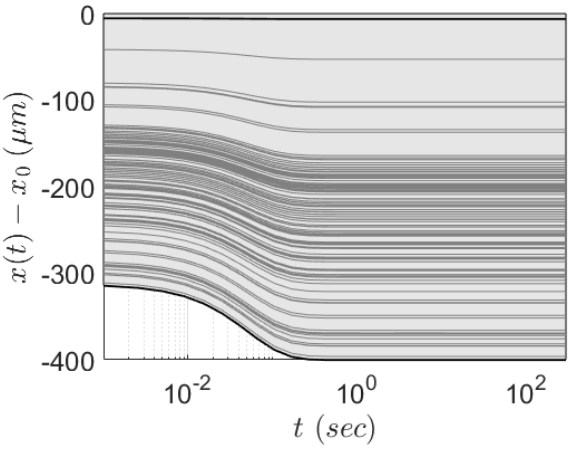

Figure 18: Displacements at P=2.5 kPa.

Diameter reduction and branch parameters Correlations were investigated using scatterplots (fig. 19). The skin was compressed in the X direction. We observed on scat-

terplots radius reduction $(r_f - r_0)/r_0$, initial radius r_0, initial cross-section X x_0 and initial cross-section angle with the X axis θ_0. The diagonal plots show the distribution for each parameter.

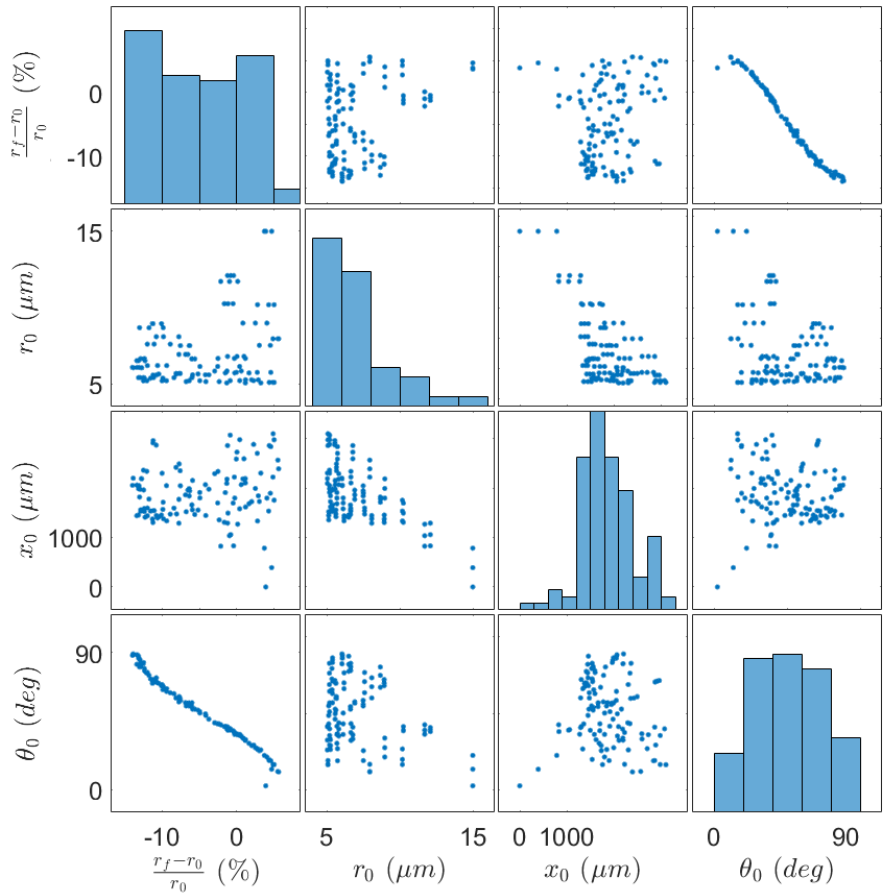

Figure 19: Scatterplots of radius reductions and branch parameters at P=2.5 kPa.

Histograms show a non-uniform distribution of r_0 and x_0 because we built the vessel as a tree. The initial radius r_0 correlates strongly with the position x_0 as the tree branches grow thinner towards the top. The radius reduction $(r_f - r_0)/r_0$ highly depends on the initial orientation θ_0. We observe diameter reduction is at its highest when vessels are at a 90° orientation and its lowest at 0°.

Branch reorientation Similarly to r, the initial branch direction represented by θ, the cross-section angle with the X direction, is time-dependent. Branches tended to reorient perpendicularly to the X direction (figs. 20 and 21). The reorientation continued after the instantaneous deformation during viscoelastic creep (figs. II.20(b) and II.21(b)). If pressure were to increase again, blood vessels would have a worse initial direction. The only cross-section that appeared to orient itself along the X axis was the first cross-section of the first

branch with some of its points constrained in displacement (fig. 20). We considered this an error of the model resulting from the boundary conditions.

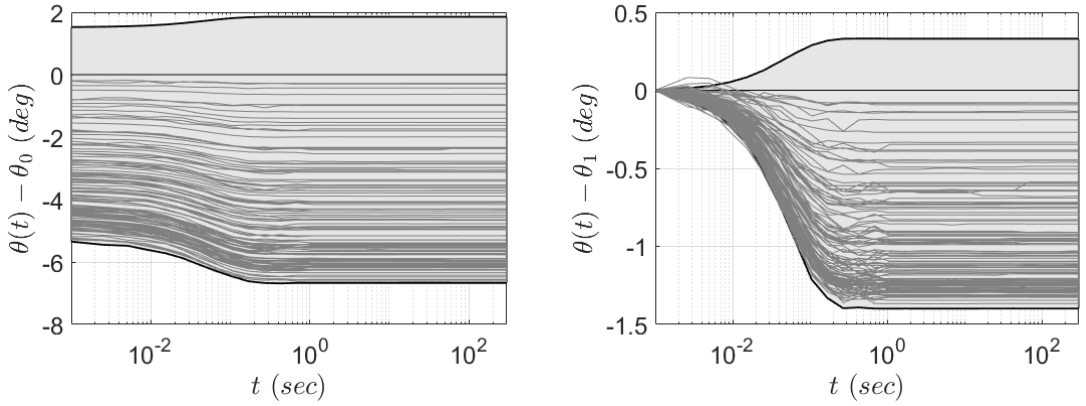

(a) Absolute branch reorientation.

(b) Normalized branch reorientation, excluding instantaneous deformation.

Figure 20: Branch reorientation versus time at p=2.5 kPa. The single curve above 0 is due to an error.

At high pressures, the change in vessel angle increased (fig. 21).

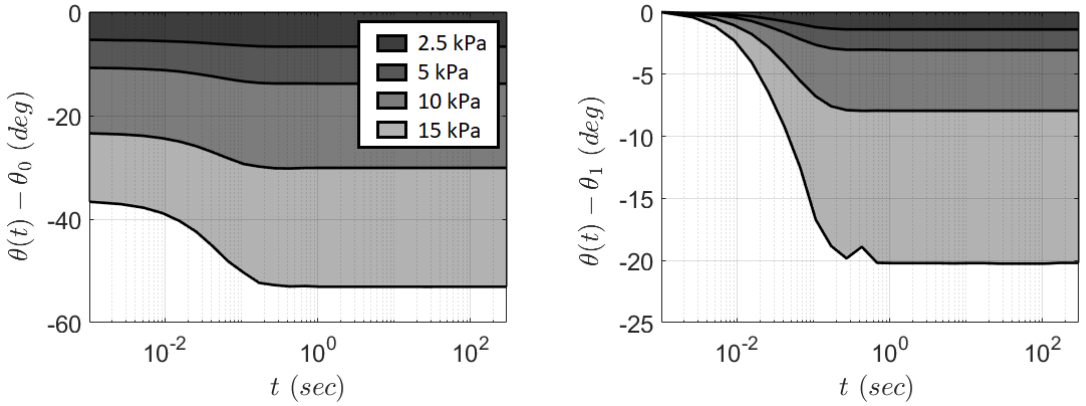

(a) Absolute branch reorientation.

(b) Normalized branch reorientation, excluding instantaneous deformation.

Figure 21: Branch reorientation versus time at p = 2.5, 5, 10, 15 kPa.

While radius change was at its highest at θ=90°, reorientation was maximal at an in-between value (49° at 2.5 kPa, fig. 22). Unlike radius reduction, reorientation distribution was not uniform but skewed, with most vessels experiencing large reorientation. While the angle, angle change, and radius change were correlated, their relationship appeared nonlinear (fig. 22).

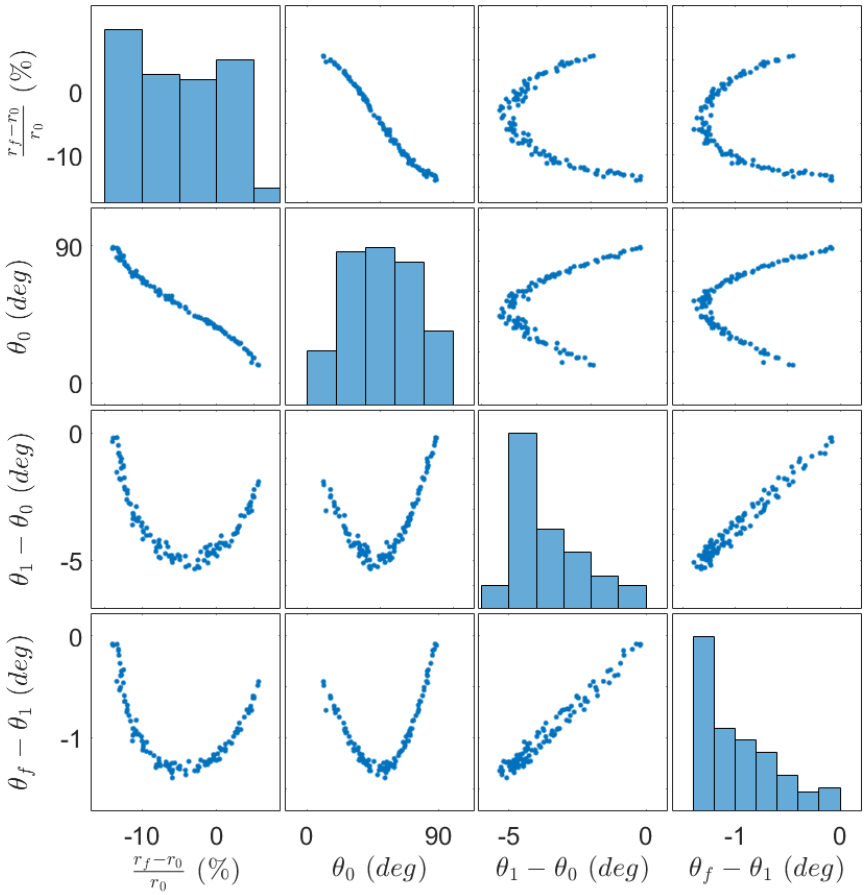

Figure 22: Scatterplots of radius reduction $\frac{r_f - r_0}{r_0}$, initial angle θ_0 and θ changes at t_1 and t_f. We observe strong non-linear correlation between the values. The reorientation is maximal at $\theta_0 \approx 49°$. As shown on their histogram, angle change is skewed.

Nonlinear effects of pressure Our material constitutive models were linear and isotropic. Radius change due to the instantaneous displacement was linear. In that time scale, all materials behaved elastically. Nonlinearity appeared as we increased pressure on the dermis when we observed radius change after the initial displacement. A cause of nonlinearity could be vessel reorientation, worsening radius change if the material exhibits viscoelastic behavior (fig. 23). Branch at 0° angle with X had their radii augmented. The radii of branches with orientations higher than 45° diminish. Finally, above a certain angle which value correlates with pressure, the reorientation became limited. Instantaneous reorientation is the first to recede while viscoelastic reorientation remains near 90° (fig. 24).

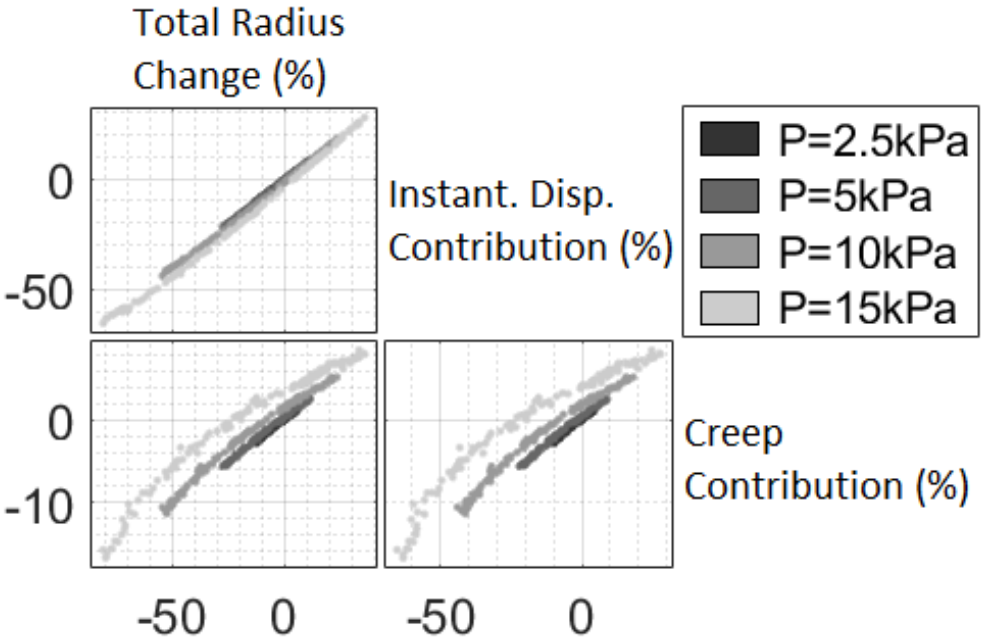

Figure 23: Radius change according to time. Radius change at t_1 due to the instantaneous displacement is mostly linear. Radius change between t_1 and t_f is non linear.

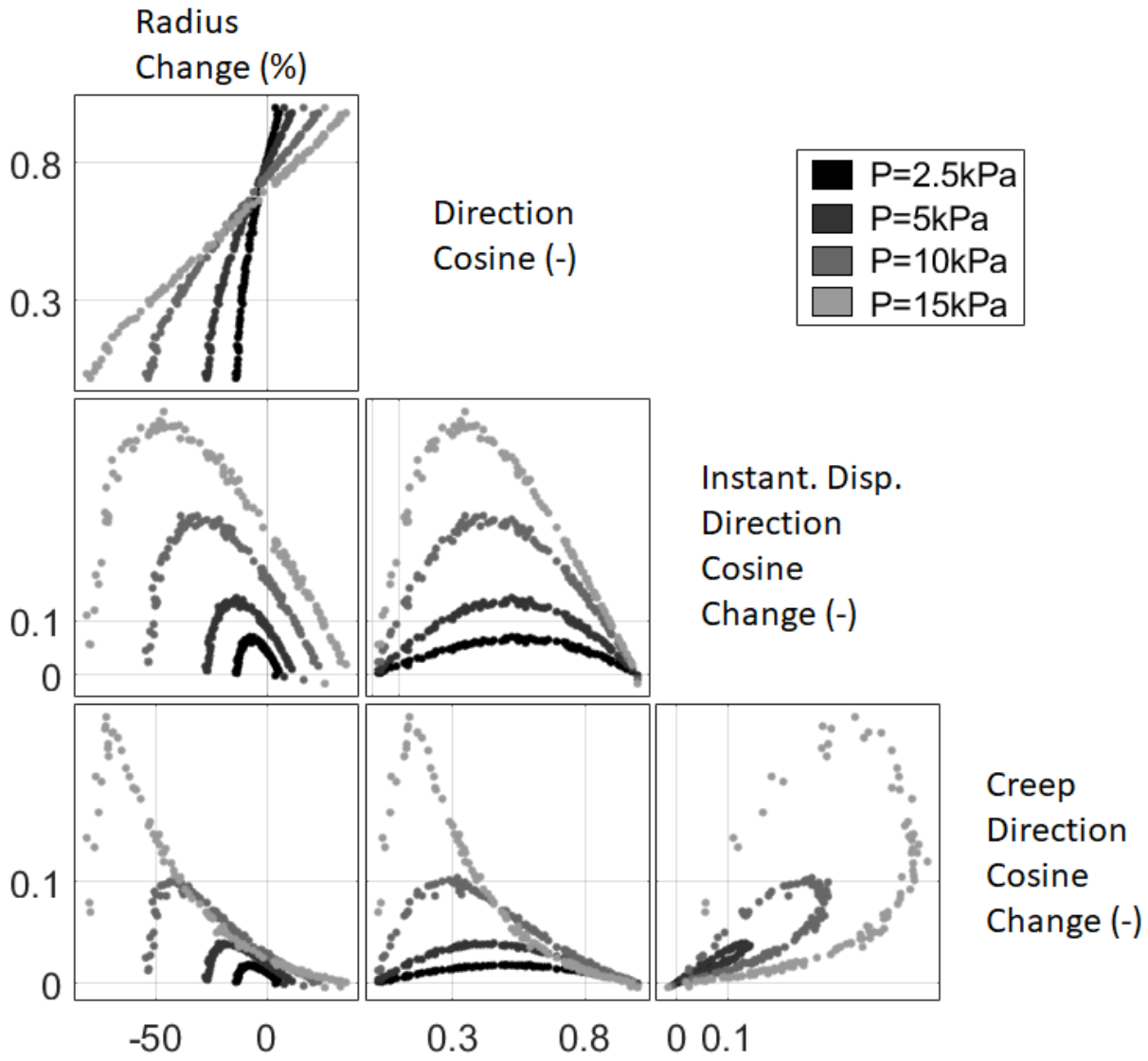

Figure 24: Radius change and direction cosine $cos(\theta)$.

2.5 Conclusion

New Knowledge Viscoelasticity has two effects on PU onset:

- viscoelastic deformation deforms the blood vessel cross-sections potentially leading to ischemia
- blood vessels reorient with time at angles worsening cross-section deformation

Work done We built a fractal blood vessel tree. We determined parameters to simulate the viscoelastic deformation of the blood vessels. We set up a method to link mesh deformation to PU onset. We reported the effect of viscoelasticity on PU onset.

Blood vessel tree Branch orientation was the most relevant property of the tree in the simulation. We had to increase mesh roughness to preserve resources to simulate the whole tree. We did not have to. We could have simulated just one blood vessel more accurately at different angles and pressures. The tree would then have two actual use: (i) for complex simulations involving not just mechanics but also chemistry or fluid dynamic, (ii) to visualize the effects of blood vessel parameters linked to specific conditions or pathologies.

Skin parameters and models We simulated a simple model using several approximated values. Modeling the dermis mechanical behavior is difficult as there are many models and parameters, but their applicability is limited. Our model should nonetheless be improved to include effects that might change blood vessel reorientation, such as anisotropy. If we use a simpler geometry, we could instead focus on more elaborate models. A simpler geometry could also help analyze the effect of different material parameters.

Detecting ischemia A definitive injury threshold might not exist. We can link hypoxia to blood vessels cross-section using the information on blood flow. By simulating a vessel instead of the whole tree, we can obtain a more accurate cross-section geometry. We can also directly reuse geometries of other studies with our knowledge of viscoelasticity and that only cross-section direction matters.

Future work We now understand how viscoelastic behavior may increase PU risk. We cannot give an injury threshold. With a new focus, a simpler geometry, and more accurate models, we can contribute new knowledge by selecting other parts of the human body susceptible to PU.

CHAPTER III

MODELLING THE LOCAL CREEP IN LCEs

3.1 Liquid Crystal Elastomers

Liquid crystal elastomers (LCEs) belong to the class of smart elastomers. Smart materials are materials designed to change their properties in response to an external stimulus, such as strain, heat, light, or humidity. Elastomers are flexible networks of polymer chains, meaning their glass transition temperature is lower than room temperature and that they present themselves in the rubbery phase at room temperature.

3.1.1 Composition of LCEs

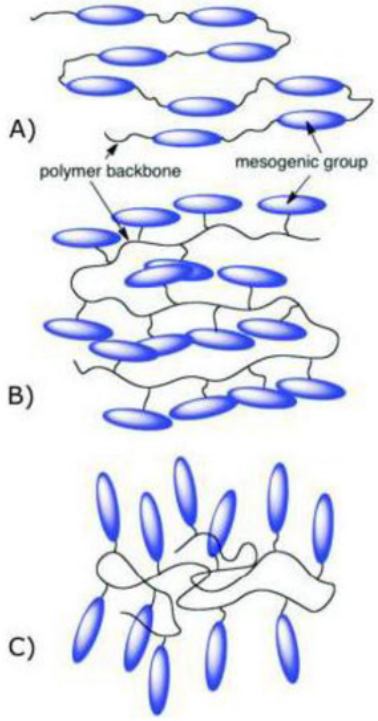

Figure 25: Mesogen positions in LCEs [36].

In LCEs, mesogens are attached to crosslinked polymer chains (fig. 25). Mesogens are responsible for the LCEs liquid-crystalline behavior. Mesogens are molecules that tend to orient themselves with respect to each other. They can form different microstructures according

to thermodynamic and loading conditions (fig. 26). In the case of thermally-activated mesogens, mesogens form an ordered – nematic – structure when the temperature is below the nematic-isotropic transition temperature T_{ni}. Above the T_{ni} temperature, mesogens are randomly oriented, the LCE is in the isotropic phase, meaning microscopically and macroscopically isotropic. Below T_{ni}, mesogens naturally arrange themselves in ordered subdomains of a few micrometers; the LCE is then in the polydomain phase. The mesogen orientation in each subdomain is random. Thus the LCE is microscopically ordered but macroscopically isotropic. Finally, when all subdomains present a unique orientation, the LCE is in the monodomain phase; it is microscopically ordered and macroscopically anisotropic.

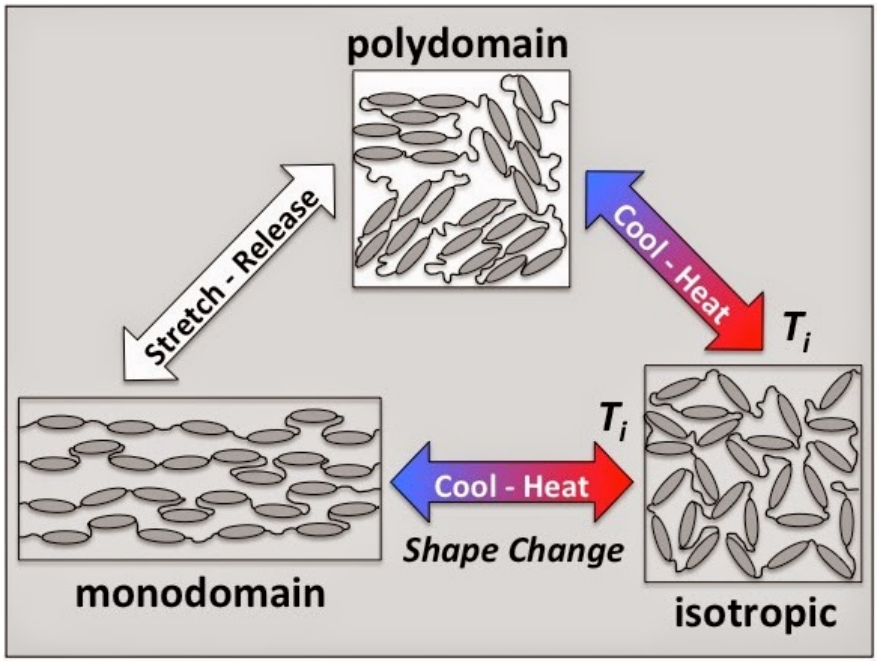

Figure 26: Phases of LCEs according to temperature and mechanical loading [46].

3.1.2 Polydomain-monodomain transition and soft elasticity

Polydomain LCE changes to monodomain when uniaxially stretched (fig. 26). This phenomenon is commonly named polydomain-monodomain (PM) transition. PM transition manifests itself in multiple changes of LCE properties.

Visually, polydomain is opaque; monodomain is transparent and birefringent. Polarized optical microscopy allows observing monodomain orientation. Monodomain LCE is transparent to polarized light when oriented at 45° with the cross-polarizers and opaque otherwise. Monodomain orientation has also been observed with wide-angle X-ray scattering methods.

LCEs mechanical behavior of evolves through the PM transition as well [6]. PM transition typically occurs in uniaxial tension (fig. 27. Past a strain threshold, the nematic directions of the subdomains rotate toward the direction of the strain. Mesogens rotation happens at no or meager cost in stress, leading to increased strain at constant stress. This highly nonlinear phenomenon is called *soft elasticity* and translates into a plateau on the stress-strain curve during the PM transition.

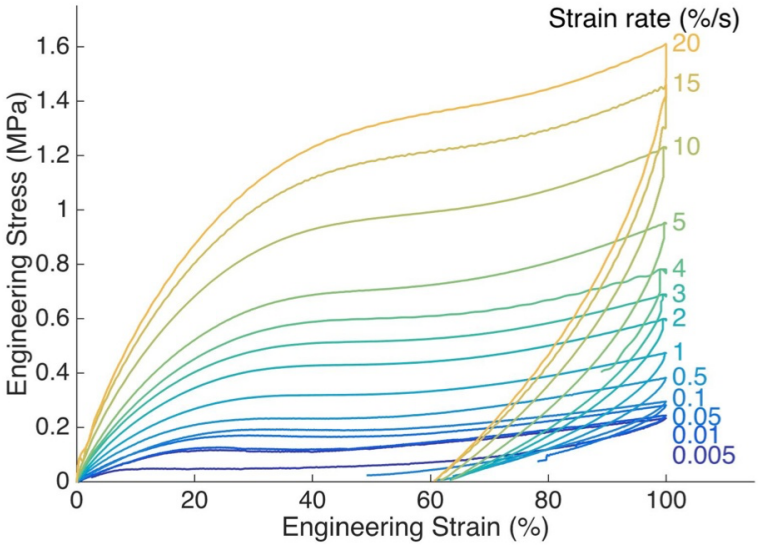

Figure 27: Soft elasticity in a main-chain LCE under uniaxial tension according to strain rate [6].

The soft elastic behavior is time-dependent in the sense that the LCE is viscoelastic (fig. 27. However, although the soft elasticity is a nonlinear phenomenon, the viscoelasticity of the material remains linear [6].

3.1.3 Viscoelastic mechanical behavior in compression

Most measurements on LCEs have been performed in tension. Indeed, uniaxial tension creates a uniform monodomain, which allows reaching high actuation strains. In this study, however, we are interested in the behavior of this highly nonlinear material in compression.

A uniaxial compressive strain applied on an incompressible material leads to a radial tensile strain. Mesogens then orient in a radial, regular but non-uniform, direction [2]. Their orientation has been demonstrated using wide-angle X-ray scattering (WAXS) measurements of a compressed specimen in different directions (fig. 28). A ring of reflection in the WAXS measurement indicates an isotropic material. These observations show compressed LCE remains isotropic in the X-Y direction but shows distinct preferred orientation in the Y-Z and X-Z planes.

The stress-strain curve of the LCE in compression also exhibits a soft elasticity plateau (fig. 29). The plateau, however, tends to appear at a lower strain threshold than in tension. So while the tension stress-strain curve exhibits three zones: polydomain, PM transition, and monodomain, indicated by three distinct slopes, the compression stress-strain curve exhibits only two zones, which are attributed to PM transition and monodomain. As in tension, the orientation under compressive loads leads to a stiffening of the material when further strain is imposed.

There has not been in the literature a comprehensive evaluation of the viscoelastic behavior of LCEs in compression. A limited number of measurements of the behavior in compression at two strain rates have recently been performed on 3D-printed lattices in order

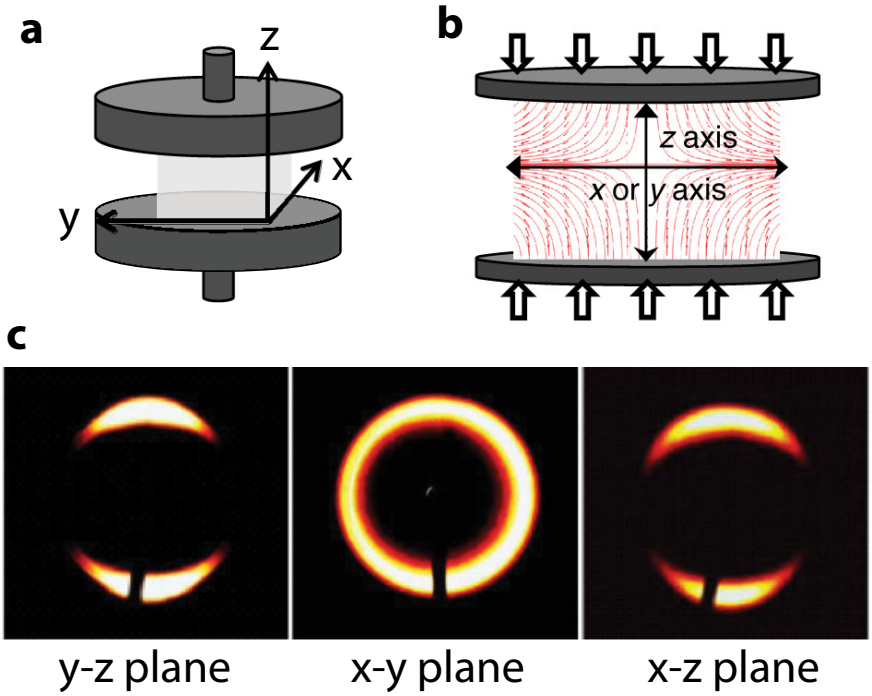

Figure 28: Experimental measurements of mesogen orientation in a specimen under uniaxial compression [2], (a) schematic of the experiment and axes, (b) representation of mesogen orientation in the specimen, (c) WAXS measurements of the specimen in three orthogonal planes.

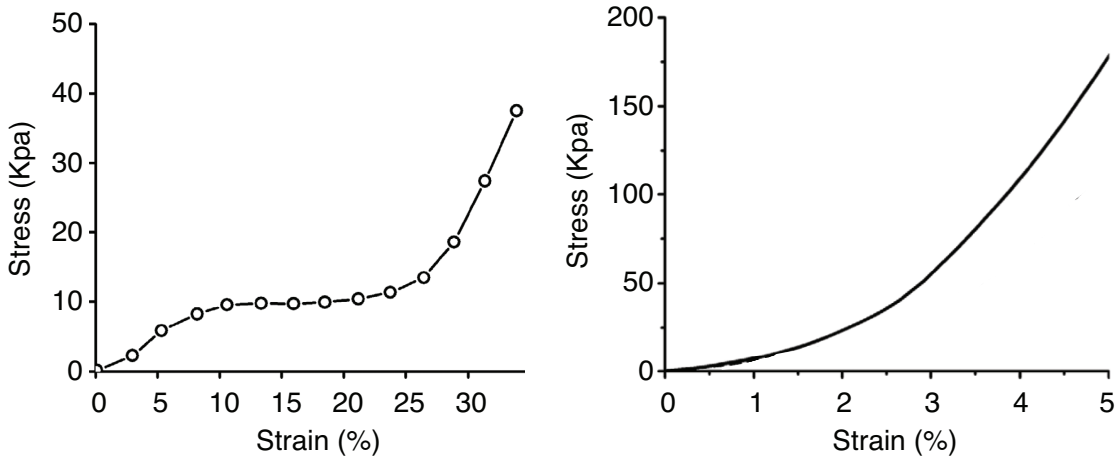

Figure 29: Example of typical experimental measurements of the stress-strain curve under uniaxial tension (left) and compression (right), measured on the same LCE composition [2].

to evaluate their damping abilities [42].

3.2 Motivation and Objectives

This study explores the behavior of LCEs under compressive creep. As a majority of LCE literature studies on their behavior in tension, we develop an experimental setup and a simulation focusing on the behavior in compression. LCEs deformation is highly nonlinear and includes specific phenomena such as soft elasticity resulting from the PM transition. We aim at understanding the PM transition in compression – where and when it happened in our Smart Skin. Experimentally, we could not directly observe PM transition as it happened inside the Smart Skin, but we could rely on other methods. To fully understand the mechanical behavior, we attempted to use an LCE constitutive model currently in development.

Objectives

- Contact simulation:
  Simulate the heel on LCE, including contact and nonlinear behavior of the LCE.
- Experimental data:
  Map pressure distribution within LCE in an experimental setup mimicking the Smart Skin under a bony prominence.
- Model evaluation:
  Help the development of the LCE model

3.3 Numerical model

3.3.1 Simulation without contact

Our goal was to simulate a viscoelastic object in contact with a rigid object. Contact problems are mechanical problems where two or more objects are in contact. However, both viscoelasticity and contact mechanics may induce convergence issues. We thus simplified the simulation by removing the contact. We modeled an LCE cylinder under compression from a disk of smaller diameter with constant pressure. The radius and height of the cylinder were chosen as four times the disk radius to neglect boundary effects (fig. 30). The bottom of the cylinder was only able to move horizontally. We simulated both creep and stress relaxation via either a constant pressure on the disk or a displacement constraint. The simulations evaluated the stress and strains over the first hour.

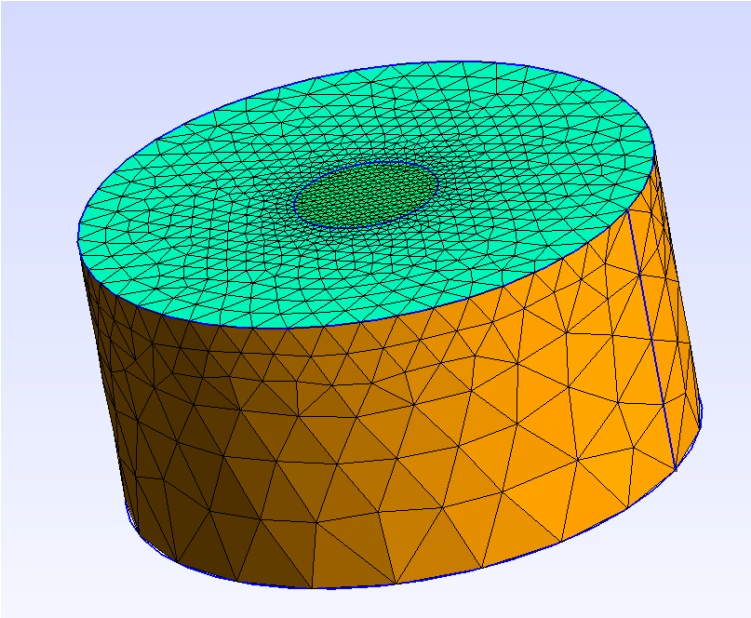

Figure 30: 3D simulation mesh, no contact.

3.3.2 Numerical method for contact problems

Contact mechanics take into account that the contact surface varies with time. A most simple contact problem is the Hertz contact problem [20], which is the contact between two spheres. An analytical solution to the Hertz contact problem exists for elastic isotropic materials. The contact between the heel and the LCE is similar to the geometry of the Hertz contact problem. However, we did not have access to an analytical solution for our specific LCE nonlinear viscoelastic behavior.

We aimed to predict the complex behavior of the LCE in contact with a rigid sphere representing the heel through the finite element method, using the software FEAP [41]. Due to software limitations, we could not define the heel as a rigid object. Thus, it has been

meshed and defined as elastic with a modulus significantly higher than the LCE. FEAP imposes contact constraints using the PENALTY or the AUGMENTED LAGRANGIAN method:

- The PENALTY method imposes the contact by modeling springs at the contact nodes. The stiffness of the springs, hence the value of the penalty, is directly linked to material parameters.
- The AUGMENTED LAGRANGIAN method uses the Lagrange multiplier method and an optional penalty term (augmentation).

To allow the stiffness tangent to converge, we gave specific instructions to FEAP. We first assigned time proportional commands to limit penetration of the heel within the support. Contact mechanics and viscoelasticity both need additional iterations to converge.

3.3.3 Comparison between 3D and axisymmetric prediction

We simplified the contact simulation by reducing the dimensions from 3D to 2D axisymmetric. To validate the use of an axisymmetric model, we compared the predicted response of the LCE from a full three-dimensional simulation and an axisymmetric simulation under similar loading. The geometry was composed of a sphere representing the heel, in contact with a thick rectangular sheet of LCE, representing the support. The heel was model as a half-sphere composed of a linear isotropic elastic material with a high elastic modulus of E =1000 GPa, so we could be neglect its deformation compared to the support. The LCE was modeled as isotropic linear elastic, with a modulus of $E = 1\ MPa$ and a Poisson's ratio of $\nu = 0.5$ for incompressibility. We chose the dimensions of the support much larger than the sphere to simulate an infinite sheet.

We meshed heel and LCE support 3D geometry with tetra elements. The 2D geometry represented half a cross-section of the geometry, which modeled a 1 rad slice and assumed axisymmetric behavior. We meshed the 2D support geometry with quad elements, while the heel used tri elements (fig. 31).

We fixed the bottom of the support in the vertical direction. Then we fixed one point in all directions to prevent rigid body motions. We divided heel displacement into steps to help convergence.

At each step of the 3D simulation, we exported the stress and strain in each element. We made 2D axisymmetric simulation to reach similar displacement levels to facilitate comparison. We sliced the 3D geometry at its center and interpolated the values of the strain and stress fields at points corresponding to the 2D nodes.

3.3.4 LCE constitutive model

We updated our material with a more realistic LCE model after performing the simulations with simple linear elastic and linear viscoelastic models. Simulations benefited from a constitutive model currently developed by Leila Rezaei in the MS2M lab. The model predicts the mechanical behavior of LCEs at room temperature, including soft elasticity and viscoelasticity. As this model is not in the public domain yet, we give a brief overview here. We took

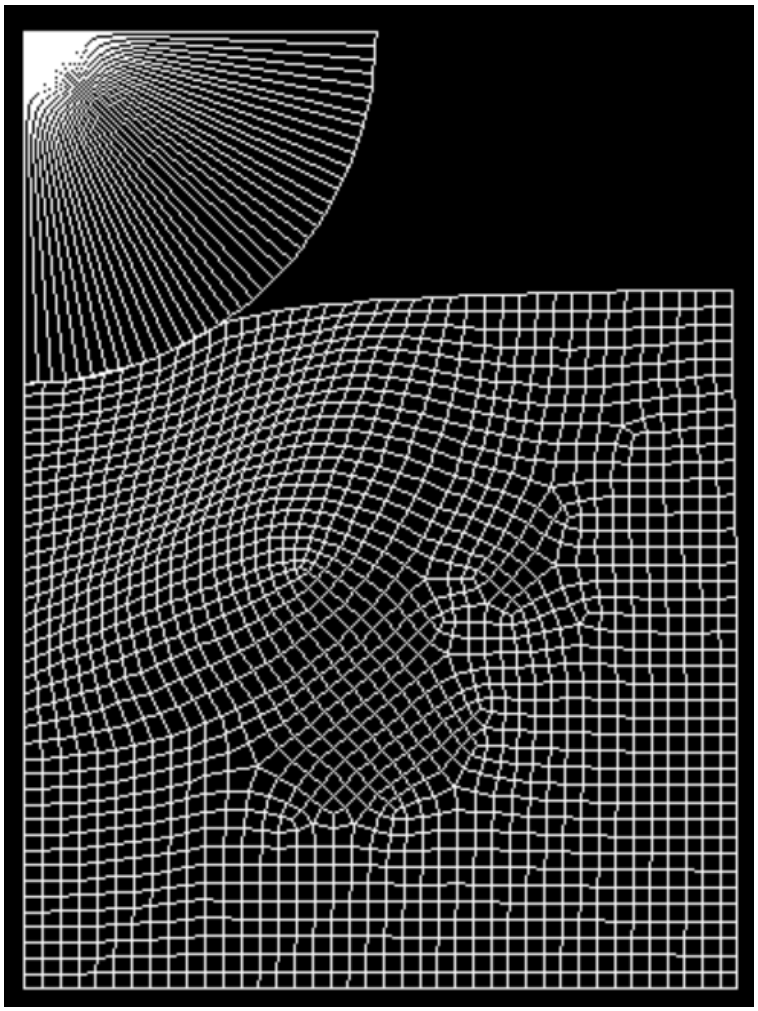

Figure 31: 2D axisymmetric deformed mesh with contact.

inspiration for our model in the representation of superelasticity with shape-memory alloys [5, 4]. An internal variable e_{tr} represents the deviatoric transition strain and keeps a record of the transition history between the polydomain and the monodomain. A linear viscoelastic generalized Maxwell model is integrated into the model to account for time-dependent effects.

Parameters of the model have been identified on experimental stress-strain curves for LCE under uniaxial tensile strain at multiple strain rates and at room temperature (fig. 32).

3.3.5 Simulation of PM transition

We can detect PM transition from experiments by the change in opacity of the specimen. To compare experiments and simulation, we needed to assess the material transitioned from polydomain to monodomain as predicted by the simulation. Mesogens align in the direction of the applied strain, along the stretch in tension, and the radial direction in compression. At each time step, we computed the principal strains in each element. If the norm of the maximum strain was higher than the threshold determined by the model, we could consider

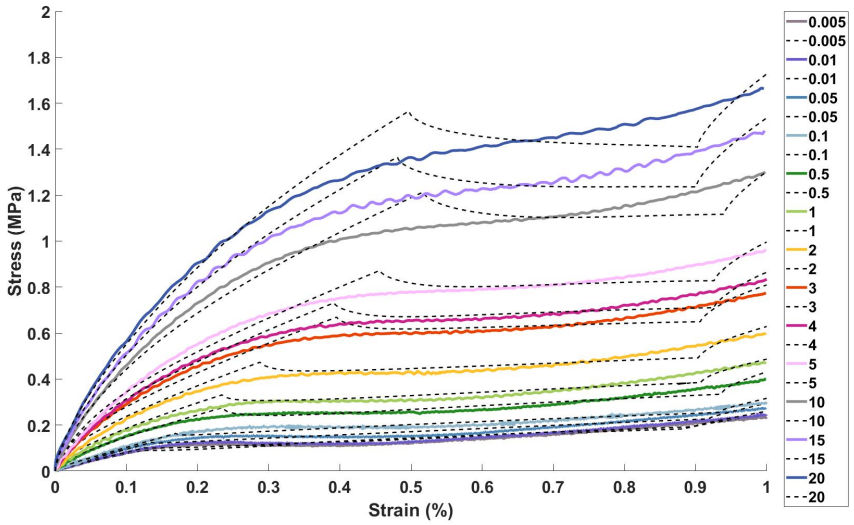

Figure 32: Comparison of model prediction with experimental measurements at multiple strain rates (Leila Rezaei).

the element transitioned to the monodomain.

3.4 Experimental methods

3.4.1 Specimen preparation

Following the method described in [46], we synthesized 25%-crosslinked UV-sensitive LCEs, using the chemicals listed in table 6.

Name	Function	Molecule
RM257	Mesogen	1,4-Bis-[4-(3-acryloyloxypropyloxy)benzoyloxy]-2-methylbenzene
EDDET	Spacer	2,2-Ethylenedioxy diethanethiol
PETMP	Crosslinker	pentaerythritol tetrakis (3-mercaptopropionate)
HHMP	Photoinitiator	(2-hydroxy-4'-(2-hydroxyethoxy)-2-methylpropiophenone)
Dipropylamine	Catalyst	Di-n-propylamine
Toluene	Solvent	-

Table 6: Chemicals involved in LCE synthesis.

We dissolved RM257, EDDET, and PETMP in toluene. An excess of RM257 compared to stoechiometric conditions was added to the mix to allow for photocuring. The mix was placed in an oven at 80°C to facilitate the dissolution. Photoinitiator (0.5%wt of the monomer) and catalyst (1 $mol\%$ of the thiol groups) were then added and mixed. The mix was placed in the oven under vacuum at 67.7 kPa (508 $mmHg$) to remove any air bubbles. Finally, we poured the obtained solution into cylindrical molds of diameter 10 mm. We cut these molds from PVC tubes, laid them on a glass plate, and sealed possible bottom leaks with vacuum grease. The solution was left 24 hours to cure at room temperature, leaving time for the thiol–acrylate reaction to occur in the swollen LCE. Finally, molds containing the solution were placed in the oven at 80°C under a vacuum of 67.7 kPa to evaporate the solvent.

Considering the shape ratio of these specimens, about 12 days were necessary to evaporate the toluene fully. Specimens initial diameter and height were measured with a caliper (table 7). P1 and P2 indicate specimens used for classic compression creep tests. We dedicated specimens 1 to 6 to the study of the PM transition during compression creep.

Specimen	P1	P2	1	2	3	4	5	6
Diameter (mm)	10	10	9.95	10.10	10.05	9.75	10.08	9.62
Height (mm)	10	4.25	8.08	9.02	7.37	8.41	8.53	6.85
Oven time (days)	15+	15+	11	12	12	13	13	13
Compression time (min)	-	-	60	15	30	15	30	60
Frozen	No	No	Yes	Yes	Yes	No	No	No

Table 7: Specimen Characteristics

All specimens contained a photoinitiator to allow for a second crosslinking in a deformed configuration. The photoinitiator was responsible for a second crosslinking when exposed to UV light, imprinting the deformation and locking the PM orientation.

3.4.2 Creep compression test

Creep compression tests were performed on specimens P1 and P2 at room temperature on an Instron 5965 (Instron, Norwood, MA, USA) equipped with a 5 kN load cell. Because we can only send displacement commands to the tensile machine, we performed preliminary testing to determine the PIL controller parameters (P: 0.1 N/mm, I:10 s, L:200 Hz). We manufactured a specific compression platen to apply uniaxial compression with a spherical end of radius smaller than the specimen. From now on, we will refer to this compression platen as the punch. We applied stress to the specimen within 2 *sec*. We obtained platen displacement through time and computed engineering strain as the ratio of displacement and initial height.

3.4.3 PM transition under creep

Scale of the experiment We made a 3D scan of a human heel using a mobile 3D scanner, Structure Sensor (Occipital, Boulder, CO, USA), mounted on an iPad (Apple, Cupertino, CA, USA). 3D scans are limited to the outside volume of an object. They are not an X-ray, which would contain information about tissue distribution in the heel, such as calcaneus bone, adipose tissue, and skin. An Object File model of the outside volume was thus obtained and exported (fig. III.33(a)). We chose an intersection plane to represent the bonny prominence on which patients would apply pressure when lying down (fig. III.33(a)). Finally, we obtained the heel profile (fig. III.33(b)). We approximated the radius of curvature at 25 mm (1 $inch$).

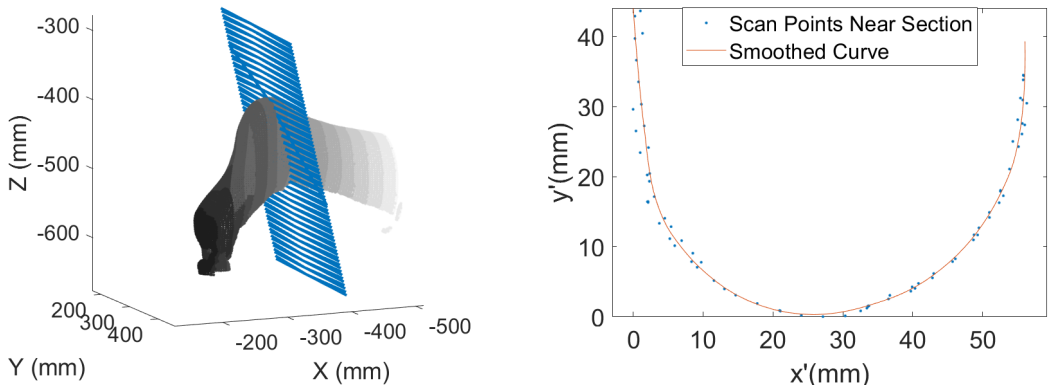

(a) Heel scan and intersection plane

(b) Heel profile

Figure 33: Human heel geometry and profile.

The size for LCE specimens synthesized in the lab was limited. The increased volume would have made solvent evaporation practical. The model experiment of the rigid heel on the LCE support is thus scaled-down. We chose 10 mm as a reasonable dimension for the cylindrical specimen.

In addition, the whole experiment was made axisymmetric. The heel was modeled as a spherical indenter of radius $r_{punch} = 2\ mm$. We chose this radius to be small enough compared to our LCE specimen diameter representing the support to neglect boundary effects.

Constant pressure setup To make creep measurements, we applied a constant load on the specimens, similarly to the weight of the heel on a support 35. We achieved this in the experimental setup by using pistons linked to the compressed air network and controlled by pressure gauges.

Spherical indenter pressure The pressure under the sphere P_s was then related to the pressure at the top of the punch P. For an isotropic material, this relation would be defined by equations (3.4.1) and (3.4.2) (fig. 34) [21].

$$P_s = \frac{3Pr^2}{2a^2} \tag{3.4.1}$$

$$a = r\left(\frac{3P\pi\left(\frac{1-\nu_1^2}{E_1}+\frac{1-\nu_2^2}{E_2}\right)}{4}\right)^{1/3} \tag{3.4.2}$$

where r is the radius of the sphere, a is the contact area, E_1 and ν_1 the Young's modulus and Poisson's ratio of the sphere, and E_2 and ν_2 the Young's modulus and Poisson's ratio of the plane. Consequently, the peak pressure P_s under the sphere is not the same as the pressure

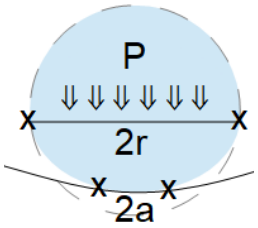

Figure 34: Hertzian contact between a sphere and a plane

P on the sphere mid-section. To define a pressure level for the experiment and characterize the LCE in creep, we arbitrarily chose the mid-sphere pressure as 50 kPa to be in a similar order of magnitude as the pressure responsible for heel PUs and to be controllable with our equipment.

Piston pressure The input pressure P_{input} of the piston is also not the same as the pressure P_s due to the 24 mm cylinder diameter in the piston and the 4 mm punch diameter. Since the force is transmitted, $F_{cylinder} = F_{punch}$, the relationship between the pressures is defined by equation (3.4.3).

$$P_{input} = P_s\left(\frac{D_{punch}}{D_{cylinder}}\right)^2 \tag{3.4.3}$$

Experimental protocol All specimens were uniaxially compressed at 1.4 kPa (0.2 psi) using a model M24 Airpel anti-stiction air cylinder (Airpot, Norwalk, CT, USA) with a bore of 24 mm, corresponding to an equivalent pressure at the diameter of the punch of 49.64 kPa (7.2 psi). We applied constant pressure for 15 min, 30 min, and 60 min to observe the viscoelastic behavior as most of the viscoelastic creep strain occurs within the

first hour (see results of creep compression tests fig. fig:Creep). We repeated each test twice. Specimens were cured at the end of the creep time in their deformed state to "lock" the PM transition. We shined UV light from the side and bottom of the specimen for 15 *min* while under pressure and 15 *min* with the pressure removed (fig. 35).

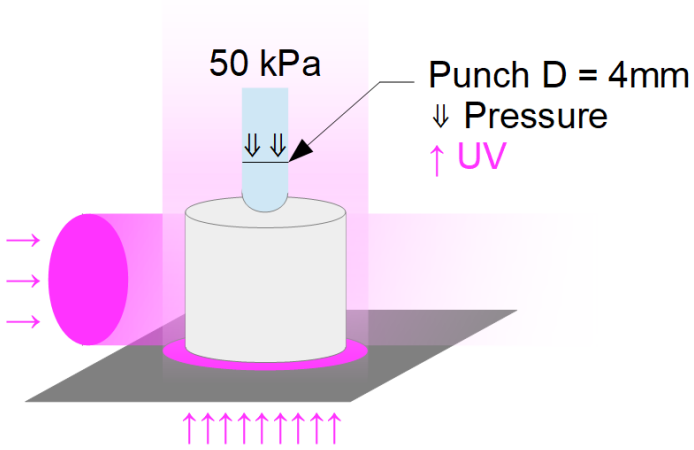

Figure 35: Simultaneous compression and curing on a specimen

Cutting the specimens to obtain a flat surface at the center proved challenging. To achieve this, we hammered a razor blade to produce an instantaneous high force (fig. 36). Hits avoided pressing the blade for any period of time, which would allow the soft material to deform during cutting. Each specimen was cut in 5 slices roughly 2 *mm* thick each (fig. 3).

Figure 36: Cutting

Determination of polydomain-monodomain phases

Optical methods can be used to determine polydomain and monodomain phases, as polydomain LCE is opaque and monodomain LCE is transparent. Additionally, polarized optical microscopy can be used to observe a change in birefringence of the monodomain from clear at 45° to dark at other polarization angles with reference to the nematic direction. The monodomain orientation in tension was successfully observed under polarized light. However, despite the transparency of the compressed specimens, nematic orientation could not be observed with polarized optical microscopy, probably because of a lack of homogeneous orientation in the specimen.

We acquired numerical pictures of the specimens with a high-resolution camera (FLIR Blackfly S BFS-U3-50S5C) equipped with a flat-field lens. We determined the PM phases from the slice images in MATLAB. We assumed constant thickness slices, with a constant 10 mm bottom length for scale. Images were processed in MATLAB, applying a mask filtering out all the white pixels at a saturation below about 0.19. We then sharpened contrast with a moving average. We used the resulting picture to detect the boundary of the monodomain 'transparent'.

3.5 Results and discussion

3.5.1 Creep

Creep tests were performed in the same conditions as the punch tests to determine the amount of creep strain corresponding to different stress levels. Results showed a maximum creep strain between 30% and 60% for stress levels at 30 and 50 kPa (fig. 37). First, these strain levels are of the same order of magnitude as the strain levels necessary to reach PM transition, indicating the relevance of measuring soft elasticity under such pressures. Second, results indicated that most of the creep occurs in the first two hours. Although we could change this time in multiple ways, it is interestingly of the same order of magnitude as the time for PU onset. Stress-strain curves also indicated that the most pronounced viscoelastic effects would occur in the first hour, with very little added value in performing tests lasting many hours.

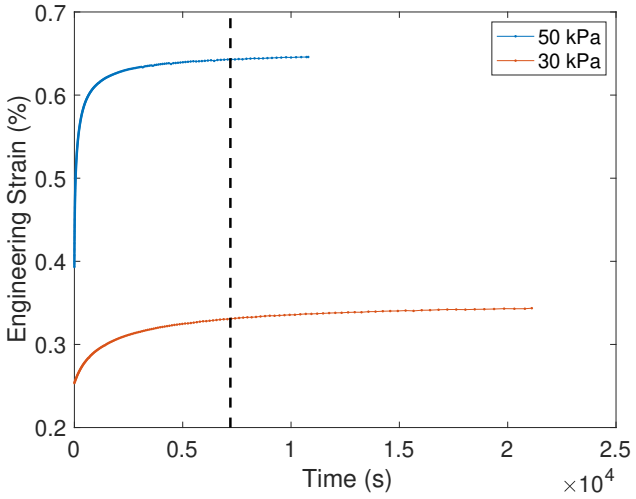

Figure 37: Creep test performed on cylindrical LCE specimens with a 4 mm punch. The dashed line indicates 2 hours.

3.5.2 Local creep and PM transition

Specimens were placed under local constant load and cured in a deformed configuration. Once cured, specimens were sliced with a razor blade (fig. 38). Cutting thin slices of constant thickness has proven challenging for this soft materials. Using machinery would modify the structure of the material.

The extent of the monodomain phase in the initially-polydomain specimen is detected and plotted in figure 39. There was a large transparent zone in all specimens, of at least 6 mm radius.

Interestingly, the zone did not seem to grow larger for specimens under longer compression. The intensity of the 'transparent' coloring on pictures was lower for short creep times of 15 min, making it harder to detect the polydomain zone. This blur could indicate the

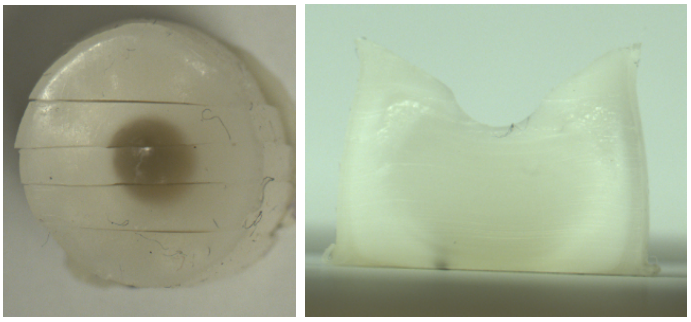

(a) Sliced specimen (b) Middle slice

Figure 38: Sliced specimen

presence of a transition zone, where the mesogens are less oriented than in a perfect monodomain. The specimens cured after 30 and 60 *min* creep show a clean boundary between polydomain and monodomain. Quantitative comparison of the size of the transitioned zone in each specimen is not possible as the monodomain zone highly depends on the initial size of the specimen and their height is not uniform.

3.5.3 Linear Elastic and Viscoelastic Models Simulation

Without contact We simulated a viscoelastic Maxwell model with three terms (3 is a software limitation) representing a polydomain LCE with no phase transition and no soft elasticity (fig. 40). We observed an expected high stress concentration at the border of the disk. Convergence was, nevertheless, not an issue, and high strains could be applied.

Contact and Validation 2D axisymmetric After simulating the contact in both 2D and 3D, we plotted the absolute error between the three-dimensional and the two-dimensional axisymmetric vertical strains (fig. 41). Results differ significantly, and we have not elucidated the reason behind this. We have noted that the mesh size significantly influences the computed error. Creating a finer 2D mesh was not an issue, but computational capacities and time limit the size of the 3D elements. We chose to use the axisymmetric model to investigate the influence of pressure on LCEs, keeping convergence rate high and computation time low.

3.5.4 LCE model, convergence, and soft elasticity

The goal of the simulation was to model the effect of the LCE soft elasticity. Soft elasticity involved a significant increase in modulus down to almost zero with an increase in loading. This drastic change in material properties in the middle of the simulation posed a particularly challenging problem when combined with contact. The PENALTY method struggled to maintain contact during the softening as the penalty depends on material modulus. Similarly, the AUGMENTED LAGRANGIAN method with and without the penalty term failed to converge as the soft elasticity began. Both 3D and 2D simulations of compressive creep exhibited the same convergence issues. We have checked that simulations run perfectly for a linear viscoelastic material. However, convergence fails as soon as we reach transition and

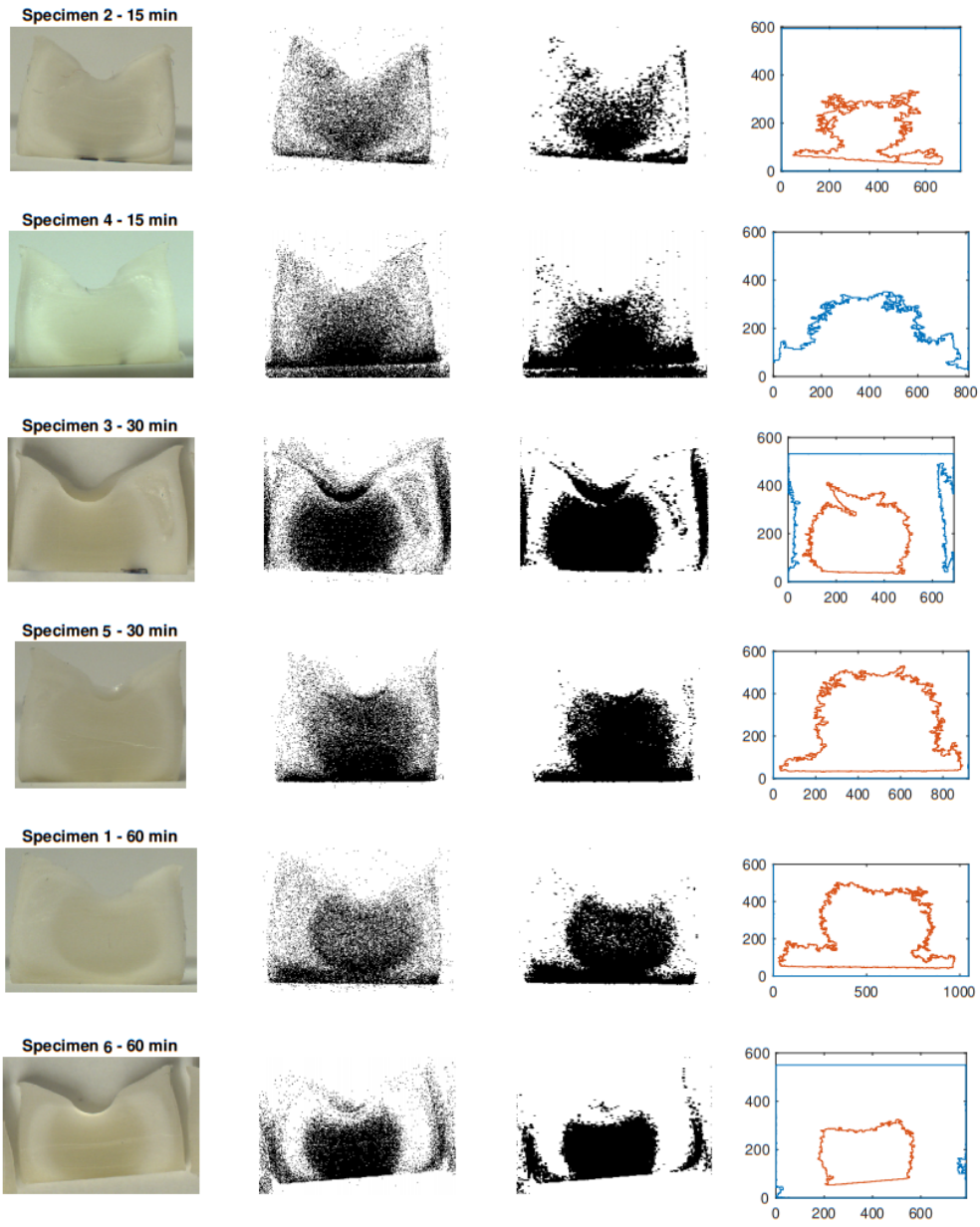

Figure 39: Detection of the PM transition on creep specimens at different durations.

soft elastic behavior. We conclude this is a logical result of how the contact is implemented in models, with a constant penalty parameter or threshold that is highly dependent on material properties. Simulating this type on nonlinearity would need an adaptive contact algorithm that will evolve with material properties.

We performed simulations without contact to relieve convergence issues. The simulations were force-driven and displacement-driven. However, they also failed to converge in the soft elasticity region, confirming that the behavior of the LCE is the challenge here, independently of the type of simulations. This failure to converge can have multiple causes. First, the model is in development and is not as robust as it could be. The constitutive law currently uses

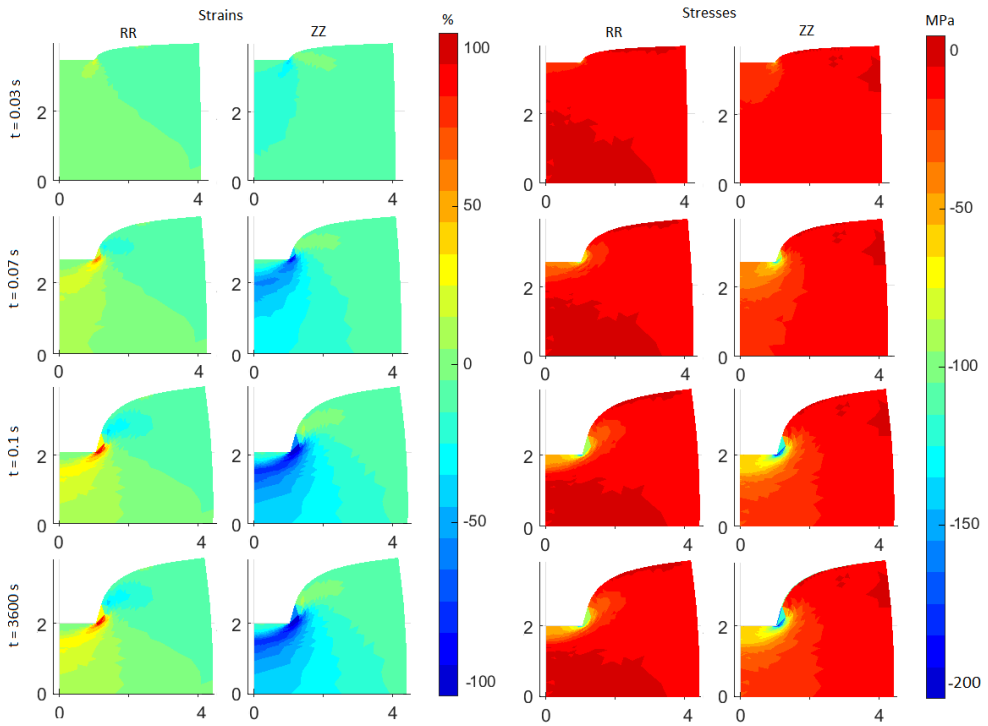

Figure 40: Stress relaxation with a linear viscoelastic material. 50% strain was reached at t = 0.1 *s* and maintained until t = 1 *hour*. Stresses and strains are plotted at different times in the axial direction (ZZ) and radial direction (RR).

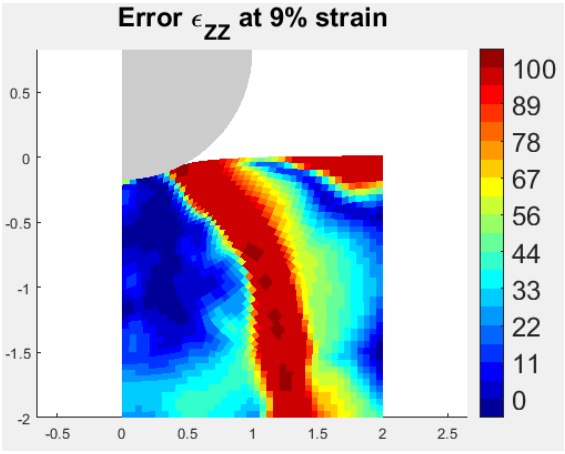

Figure 41: Absolute error in axial strain

a numerical tangent that has to overcome the soft elasticity threshold. Second, the sudden softening may lead to shape factor issues on the elements most compressed. This material would also prevent the robust computation of the tangent.

In a more general manner, this experience reflected the difficulty in performing realistic simulations of LCEs in general. These materials have been defined as a new category because they sometimes behave like a solid, sometimes like a liquid. This highly nonlinear behavior is of high interest for numerous applications but is challenging for finite element simulations.

A conclusion of this study is that other numerical methods may be more appropriate.

3.6 Conclusion

New Knowledge

- polarized microscopy is not adapted to observe PM orientation if that orientation is not uniaxial.
- we can detect the transitioned region on simple high-resolution pictures.
- 30 minutes is too long to observe the evolution of PM transition in the smart skin
- the current LCE constitutive model does not converge for large meshes.

Work done We measured the creep behavior of the LCE under a punch. The transition from monodomain to polydomain during creep was measured using pictures of LCE specimens cured during creep. We implemented finite element simulations of 3D and 2D axisymmetric elastic isotropic contact, comparing the results for the two geometries. Finally, we attempted to simulate the pressure distribution in the LCE Smart Skin under a bony prominence.

Experiment Most of the creep in the Smart Skin occurs within the first two hours, which is the recommended interval between patient movement. However, the PM transition appears to occur before 30 $mins$. We are unsure of the minimum exposition time to UV needed to cure specimens and how that impacted our observations with our current method. Faster curing would improve observations. Understanding PM transition will be crucial to understand soft elasticity and LCE behavior.

Contact Simulation Introducing contact makes the simulation more challenging. Elements are under large shear loads because of the contact geometry and LCE incompressibility. We do not find the current LCE constitutive model adapted to the numerical tangent convergence. Thus efforts should be focused on solving the tangent issue first. The model may never work with contact mechanics, but we devised several simulations to avoid it.

Model Evaluation Unfortunately, we were not able to compare numerical simulations to the experiments. The simulations failed to converge in the first steps before our proportional load reached its maximum, indicating the model predicts the onset of the PM transition relatively early in the loading process. We are now interested in knowing how fast the PM transition occurs and if it increases in creep. The shape of the punch is relevant, but experimentation on standard compression platen might yield relevent answers on the time scale of PM transition.

Future work We now have a new time range to study PM transition. We should also change our strategy to simulate and compare more straightforward experiments, thus easing the challenge of using the complex nonlinear constitutive model.

CHAPTER IV

CONCLUSION AND FUTURE WORK

We can now link skin viscoelasticity behavior to PU risk. Our model shows that the instantaneous deformation, while contributing to ischemia the most, is not enough to neglect the viscoelastic behavior. Vessel angle and pressure are the most critical parameters in determining cross-section deformation. However, vessel angle also evolves with time and can worsen the effect of subsequent loading.

We successfully built a realistic fractal blood vessel tree. The tree opens the door to future simulations of the blood vessel in the skin in contact with the LCE Smart Skin. We could use the fractal tree in more complex simulations, including ischemia chemistry or blood distribution. Such a complex geometry is not necessary to simulate cross-section deformation, and we could have modeled an oriented tube in a medium.

We calibrated the viscoelastic skin model on experimental measurements. However, we know that skin properties can differ significantly depending on many factors such as age, health, or location. This diversity in properties allows for further improvements of the model, including disparities, to obtain more detailed results on blood vessel occlusion. The implemented Maxwell model quickly reaches a maximum strain because the characteristic times included were limited to relatively low values. A complete characterization of the skin, including long-time scales, would be relevant here. If deformation were to continue, cross-section deformation might lead to further blood vessel occlusion.

We observed the PM transition in the LCE but not the expected increase in transitioned monodomain with time. Polarized microscopy is not adapted to observe monodomain heterogeneous orientation. Consequently, we have used simple optical measurements. We should shorten the UV exposure time to observe PM transition as it occurs early during the test. A time of two hours nonetheless appears to be the correct time scale to observe the Smart Skin. Simulations also yielded interesting results, showing that a numerical tangent may not be appropriate to simulate the softening of the LCE behavior.

Future work. New Smart Skin simulation should first be more straightforward and aim at simulating LCE subject to uniaxial compression. We could design an experiment to observe PM orientation in uniaxial compression with a flat compression platen. PM transition should be most noticeable in the first 15 minutes. Information on when and where the PM transition occurs will also help locate when and where soft elasticity occurs. This straightforward experiment would also lead to a simple simulation, eliminating convergence issues with contact or complex geometry/boundary conditions. A complete characterization of the PM transition and soft elasticity in compression will allow us to locate and time the soft elasticity in a potential Smart Skin. The simulation method will probably have to change

to a more adapted numerical method that does not rely on solid material. As long as soft elasticity does no occur, the finite element method is satisfactory.

REFERENCES

[1] Olivier Adjoua, Stéphanie Pitre-Champagnat, and Didier Lucor. Reduced-order modeling of hemodynamics across macroscopic through mesoscopic circulation scales. International Journal for Numerical Methods in Biomedical Engineering, 35(12):1–17, 2019.

[2] Aditya Agrawal, Alin C. Chipara, Yousif Shamoo, Prabir K. Patra, Brent J. Carey, Pulickel M. Ajayan, Walter G. Chapman, and Rafael Verduzco. Dynamic self-stiffening in liquid crystal elastomers. Nature Communications, 4(1):1739, June 2013.

[3] Karoon Agrawal and Neha Chauhan. Pressure ulcers: Back to the basics. Indian Journal of Plastic Surgery, 45(2):244–254, 2012.

[4] Ferdinando Auricchio and Robert L. Taylor. Shape-memory alloys: modelling and numerical simulations of the finite-strain superelastic behavior. Computer Methods in Applied Mechanics and Engineering, 143(1-2):175–194, April 1997.

[5] Ferdinando Auricchio, Robert L. Taylor, and Jacob Lubliner. Shape-memory alloys: macromodelling and numerical simulations of the superelastic behavior. Computer Methods in Applied Mechanics and Engineering, 146(3-4):281–312, July 1997.

[6] A. Azoug, V. Vasconcellos, J. Dooling, M. Saed, C.M. Yakacki, and T.D. Nguyen. Viscoelasticity of the polydomain-monodomain transition in main-chain liquid crystal elastomers. Polymer, 98:165–171, August 2016.

[7] Dan Bader and Cees Oomens. Recent Advances in Pressure Ulcer Research, pages 11–26. Springer London, London, 2006.

[8] José María Benítez and Francisco Javier Montáns. The mechanical behavior of skin: Structures and models for the finite element analysis. Computers and Structures, 190:75–107, 2017.

[9] Surajit Bhattacharya and R. Mishra. Pressure ulcers: Current understanding and newer modalities of treatment. Indian Journal of Plastic Surgery, 48(1):4–16, 2015.

[10] Mishra RK Bhattacharya S. Pressure ulcers: Current understanding and newer modalities of treatment. Indian Journal of Plastic Surgery, 48, 2015.

[11] Irwin M. Braverman, Agnes Keh, and David Goldminz. Correlation of laser doppler wave patterns with underlying microvascular anatomy. Journal of Investigative Dermatology, 95(3):283–286, 1990.

[12] Gregor Cevc and Ulrich Vierl. Spatial distribution of cutaneous microvasculature and local drug clearance after drug application on the skin. Journal of Controlled Release, 118(1):18–26, 2007.

[13] Clare Y.L. Chao, Yong Ping Zheng, and Gladys L.Y. Cheing. Epidermal Thickness and Biomechanical Properties of Plantar Tissues in Diabetic Foot. Ultrasound in Medicine and Biology, 37(7):1029–1038, 2011.

[14] Michiel P. De Looze, Lottie F.M. Kuijt-Evers, and Jaap Van Dieën. Sitting comfort and discomfort and the relationships with objective measures. Ergonomics, 46(10):985–997, 2003.

[15] Laura E. Edsberg, Joyce M. Black, Margaret Goldberg, Laurie McNichol, Lynn Moore, and Mary Sieggreen. Revised National Pressure Ulcer Advisory Panel Pressure Injury Staging System. Journal of Wound, Ostomy and Continence Nursing, 43(6):585–597, 2016.

[16] C. Geuzaine and J.-F. Remacle. Gmsh: a three-dimensional finite element mesh generator with built-in pre- and post-processing facilities. International Journal for Numerical Methods in Engineering, 79(11):1309–1331, 2009.

[17] Lowell A. Goldsmith. My Organ Is Bigger Than Your Organ. Archives of Dermatology, 126(3):301–302, 03 1990.

[18] Farina Hashmi, Christopher Nester, Ciaran Wright, Veronica Newton, and Sharon Lam. Characterising the biophysical properties of normal and hyperkeratotic foot skin. Journal of Foot and Ankle Research, 8(1):1–10, 2015.

[19] Baukje Hemmes, Martijn Poeze, and Peter R.G. Brink. Reduced tissue-interface pressure and increased comfort on a newly developed soft-layered long spineboard. Journal of Trauma - Injury, Infection and Critical Care, 68(3):593–598, 2010.

[20] H. R. Hertz and P. Lenard. On the contact of rigid elastic solids and on hardness. In Miscellaneous Papers, chapter VI, pages 163–183. Macmillan, 1896.

[21] K Johnson. Contact Mechanics. Cambridge University Press, 1985.

[22] Hamed Joodaki and Matthew B. Panzer. Skin mechanical properties and modeling: A review. Proceedings of the Institution of Mechanical Engineers, Part H: Journal of Engineering in Medicine, 232(4):323–343, 2018.

[23] Diane Langemo and Margaret Goldberg. Pressure Ulcers : Avoidable or Unavoidable ? Ostomy Wound Management, 57(2)(February):1–14, 2011.

[24] Dominga Lapi, Martina Di Maro, Teresa Mastantuono, Noemy Starita, Mauro Ursino, and Antonio Colantuoni. Arterial network geometric characteristics and regulation of capillary blood flow in hamster skeletal muscle microcirculation. Frontiers in Physiology, 10(JAN):1–12, 2019.

[25] William R. Ledoux and Joanna J. Blevins. The compressive material properties of the plantar soft tissue. Journal of Biomechanics, 40(13):2975–2981, 2007.

[26] Isaac P.H. Leung, Leigh Fleming, Karl Walton, Simon Barrans, and Karen Ousey. Development of a model to demonstrate the effects of friction and pressure on skin in relation to pressure ulcer formation. Wear, 376-377:266–271, 2017. 21st International Conference on Wear of Materials.

[27] Georges Limbert, editor. Constitutive Modelling of Skin Mechanics, pages 19–76. Springer International Publishing, Cham, 2019.

[28] Definition of ulcer. `http://web.archive.org/web/20210409014834/https://www.merriam-webster.com/dictionary/ulcer`, 2021. Accessed: 2021-04-09.

[29] Bit Cecil D Murray. THE PHYSIOLOGICAL PRINCIPLE OF MINIMUM WORK APPLIED TO THE ANGLE OF BRANCHING OF ARTERIES. The Journal of general physiology, 9(4):835–841, 1926.

[30] Cecil D. Murray. The Physiological Principle of minimum work, I. Vascular system and the cost of blood volume. Proceedings of the National Academy of Sciences of the United States of America, 12:207, 1926.

[31] Yoshihiro Nakamura and Shoichi Awa. Radius exponent in elastic and rigid arterial models optimized by the least energy principle. Physiological Reports, 2(2):e00236, 2014.

[32] European Pressure Ulcer Advisory Panel National Pressure Ulcer Advisory Panel and Pan Pacific Pressure Injury Alliance. Emily Haesler (Ed.). Prevention and treatment of pressure ulcers: Clinical practice guideline. Cambridge Media, 2014.

[33] S. Nicolle, J. Decorps, B. Fromy, and J. F. Palierne. New regime in the mechanical behavior of skin: strain-softening occurring before strain-hardening. Journal of the Mechanical Behavior of Biomedical Materials, 69(December 2016):98–106, 2017.

[34] William V. Padula and Benjo A. Delarmente. The national cost of hospital-acquired pressure injuries in the United States. International Wound Journal, 16(3):634–640, 2019.

[35] David Pickham, Betsy Ballew, Kristi Ebong, Julie Shinn, Mary E. Lough, and Barbara Mayer. Evaluating optimal patient-turning procedures for reducing hospital-acquired pressure ulcers (LS-HAPU): Study protocol for a randomized controlled trial. Trials, 17(1):1–8, 2016.

[36] Hegmann E. Prévôt ME, Ustunel S. Liquid crystal elastomers-A path to biocompatible and biodegradable 3D-LCE scaffolds for tissue regeneration. Materials, 11(3), 2018.

[37] Sorvillo F. Redelings MD, Lee NE. Pressure ulcers: More lethal than we thought? Advances in Skin & Wound Care, 18:367–372, 2005.

[38] J. B. Reswick and J. E. Rogers. Experience at Rancho Los Amigos Hospital With Devices and Techniques to Prevent Pressure Sores. Bed Sore Biomechanics, 2:301–310, 1976.

[39] Vivek D. Sree, Manuel K. Rausch, and Adrian B. Tepole. Linking microvascular collapse to tissue hypoxia in a multiscale model of pressure ulcer initiation. Biomechanics and Modeling in Mechanobiology, 2019.

[40] Tatsuhisa Takahashi. Microcirculation in Fractal Branching Networks. Springer, 2014.

[41] R.L. Taylor. FEAP - finite element analysis program, 2014.

[42] Nicholas A. Traugutt, Devesh Mistry, Chaoqian Luo, Kai Yu, Qi Ge, and Christopher M. Yakacki. Liquid-Crystal-Elastomer-Based Dissipative Structures by Digital Light Processing 3D Printing. Advanced Materials, 32(28):2000797, July 2020.

[43] K. Vanderwee, M. H.F. Grypdonck, D. De Bacquer, and Tom Defloor. Effectiveness of turning with unequal time intervals on the incidence of pressure ulcer lesions. Journal of Advanced Nursing, 57(1):59–68, 2007.

[44] Peter Vowden and Kath Vowden. Diabetic foot ulcer or pressure ulcer? that is the question. The Diabetic Foot Journal, 2016.

[45] Geoffrey B. West, James H. Brown, and Brian J. Enquist. A general model for the origin of allometric scaling laws in biology. Science, 276(5309):122–126, 1997.

[46] C. M. Yakacki, M. Saed, D. P. Nair, T. Gong, S. M. Reed, and C. N. Bowman. Tailorable and programmable liquid-crystalline elastomers using a two-stage thiol–acrylate reaction. RSC Advances, 5(25):18997–19001, 2015.

[47] M. Zamir. Optimality principles in arterial branching. Journal of Theoretical Biology, 62(1):227–251, 1976.

[48] Cordelia Ziraldo, Alexey Solovyev, Ana Allegretti, Shilpa Krishnan, M. Kristi Henzel, Gwendolyn A. Sowa, David Brienza, Gary An, Qi Mi, and Yoram Vodovotz. A Computational, Tissue-Realistic Model of Pressure Ulcer Formation in Individuals with Spinal Cord Injury. PLOS Computational Biology, 11(6):e1004309, June 2015.

VITA

Jeremy Perez

Candidate for the Degree of

Master of Science

Thesis: PREVENTING PRESSURE ULCERS BY PRESSURE DISTRIBUTION VIA A LIQUID CRYSTAL ELASTOMER SMART SKIN

Major Field: Mechanical and Aerospace Engineering

Biographical:

Education:

Completed the requirements for the Master of Science in Mechanical and Aerospace Engineering at Oklahoma State University, Stillwater, Oklahoma in July, 2021.

Completed the requirements for the Master of Engineering in Mechanical Engineering at École Catholique des Arts et Métiers, 67300 Schiltigheim, France in 2016.

Completed the requirements for the Bachelor of Science in Mechanical Engineering at École Catholique des Arts et Métiers, 67300 Schiltigheim, France in 2016.